Graduate School ETD Form 9
(Revised 12/07)

PURDUE UNIVERSITY
GRADUATE SCHOOL
Thesis/Dissertation Acceptance

This is to certify that the thesis/dissertation prepared

By Nan Chen

Entitled
Mechanisms of Axis-switching and Saddle-back Velocity Profile in Laminar and Turbulent Rectangular Jets

For the degree of Master of Science in Mechanical Engineering

Is approved by the final examining committee:

Yu, Huidan (Whitney)
Chair

Nalim, M. Razi

Zhu, Likun

To the best of my knowledge and as understood by the student in the *Research Integrity and Copyright Disclaimer (Graduate School Form 20)*, this thesis/dissertation adheres to the provisions of Purdue University's "Policy on Integrity in Research" and the use of copyrighted material.

Approved by Major Professor(s): Yu, Huidan (Whitney)

Approved by: Sohel Anwar 07/22/2013
Head of the Graduate Program Date

MECHANISMS OF AXIS-SWITCHING AND SADDLE-BACK VELOCITY PROFILE IN LAMINAR AND TURBULENT RECTANGULAR JETS

A Thesis

Submitted to the Faculty

of

Purdue University

by

Nan Chen

In Partial Fulfillment of the

Requirements for the Degree

of

Master of Science in Mechanical Engineering

August 2013

Purdue University

Indianapolis, Indiana

ACKNOWLEDGMENTS

My gratitude first goes to my parents, who were supportive when their only child was determined to pursue his education overseas. Ever since they have been always there to listen to me and sending me encouraging messages, which I feel are the biggest comfort for me to hold on till the completion of my program in a different country.

I am deeply indebted to my supervisor and advisory committee chair, Dr. Whitney Yu, who accepted me as one of her first two students two years ago. I might never have had the chance to start my academic endeavor in IUPUI without her financial support. Dr. Yu is an enthusiastic academic professional, both in teaching and conducting research. The appropriate pressure from her professional passion has benefited me in developing good scientific thinking, undertaking and presentation. I also appreciate her good intention in sending me to the conference meetings.

Dr. Mark Petersen from Los Alamos National Lab contributed a lot to the turbulent inlet generation part of this thesis. It was a pleasure to communicate with him regarding the problems I encountered when advancing my project. I express my thanks to the generous help from him.

I am extremely lucky to have made a few good friends. They have kept me company and helped me out through hard time, which enables me to dedicate myself to research with the best state. Spandana Gannavaram also helped proofread this thesis.

Thanks to the insight from my other committee members, Dr. Razi Nalim and Dr. Likun Zhu, this thesis gets to become one step closer to perfection.

Dr. Jie Chen recommended me to Dr. Yu when I first contacted him. I am grateful for his support sincerely.

With the helpful information and assistance from Sara Vitaniemi and Aimee Wood, I managed to fulfil all graduation requirements in time. Valerie Lim Diemer made this thesis free from formatting errors and even offered to help me with the wording and phrasing. I owe my thanks to them as well.

TABLE OF CONTENTS

LIST OF TABLES

LIST OF FIGURES

Figure Page

LIST OF SYMBOLS

B	domain spanwise dimension
b	orifice width
C	turbulence intensity adjusting factor
c	δ_x/δ_t
c_s	sound speed
D_e	equivalent diameter
Δ_{pc}	peak-center difference for saddle-back profile
E	energy spectrum
E_{des}	desired energy spectrum
$\boldsymbol{e}_i$	particle velocities
$\boldsymbol{e}_{i\alpha}$, $\boldsymbol{e}_{i\beta}$	αth or βth component of particle velocities
f_i	distribution functions
f_i^{eq}	distribution equilibrium functions
f_i^*	distribution functions of $-\boldsymbol{e}_1$
H	domain lateral dimension
h	orifice height
I	turbulence intensity for turbulent inlet velocity profile
i	imaginary unit
k	total wavenumber
k_i	wavenumbers of element in the 3D turbulence generation model
Δk	total wavenumber increment
L	domain streamwise dimension
M	transformation matrix
M_f	number of directions in the LBM model
M_n	number of directions in the LGA model

$max\{\cdots\}$	maximum value
N_1,N_2,N_3	dimensions of 3D turbulence generation model
n_1,n_2,n_3	indices of element in the 3D turbulence generation model
n_i	Boolean variables
ν	kinematic viscosity
ν_t	eddy viscosity
ν^*	effective viscosity
Ω_i	collision operator
ω_x	streamwise vorticity
ω_i	weighting factors
Re	Reynolds number
$\boldsymbol{r}$	particle displacement vector
ρ	total density
ρ_0	constant mean density, set to unity
$\rho_{u\omega}$	correlation function of sreamwise velocity and vorticity
$\delta\rho$	density fluctuation
S	$\sqrt{\langle S_{ij}S_{ij}\rangle}$
S_{ij}, $S_{\alpha\beta}$	strain rate tensor
$\hat{S}$	diagonal collision matrix
s_i	relaxation time scales
s_i^*	effective relaxation time scales
t	current time-step
δ_t	discrete time-step, set to unity
τ	relaxation time
U	mean sreamwise velocities
U_0	laminar velocity at the center of turbulent inlet
U_i	inlet laminar velocity
U_{cl}	mean centerline velocity
U_{max}	maximum mean centerline velocity

$\boldsymbol{u}$	velocity in LBM model
u	velocity magnitude in LBM model, streamwise velocity
u'	streamwise turbulence intensity
u_0	uniform inflow velocity
u_{cl}	centerline velocity
u_{max}	maximum centerline velocity
u_i	turbulent inlet velocity
u_i'	fluctuating velocity at turbulent inlet
$\tilde{u}_i'$	spectral fluctuating velocity at turbulent inlet
$\boldsymbol{V}$	secondary flow velocity
V	mean lateral velocity
V_m	secondary flow velocity magnitude
v	lateral velocity
W	mean spanwise velocity
W_h	half-width for turbulent jet
w	spanwise velocity
x	streamwise axis
δ_X	filter length scale
δ_x	lattice length, set to unity
$Y_{\frac{1}{2}}$	lateral of half-width for turbulent jet
Y_h	y coordinate of point on half-width contour for turbulent jet
y	lateral axis
$y_{\frac{1}{2}}$	lateral of half-width for laminar jet
$Z_{\frac{1}{2}}$	spanwise half-width for turbulent jet
Z_h	z coordinate of point on half-width contour for turbulent jet
z	spanwise axis
$z_{\frac{1}{2}}$	spanwise half-width for laminar jet
ζ	bulk viscosity

LIST OF ABBREVIATIONS

2D	two-dimensional
3D	three-dimensional
AD	axisymmetric decay
AR	aspect ratio
CD	characteristic decay
CFD	computational fluid dynamics
DNS	direct numerical simulation
FFT	fast Fourier transformation
HWC	half-width contour
IFFT	inverse fast Fourier transformation
LBM	lattice Boltzmann method
LES	large-eddy simulation
LGA	lattice gas automata
MSV	mean streamwise velocity
MRT	multiple-relaxation-time
PC	potential core
PSB	profound saddle-back
RMS	root-mean-square
SRT	single-relaxation-time

ABSTRACT

Chen, Nan. M.S.M.E, Purdue University, August 2013. Mechanisms of Axis-switching and Saddle-back Velocity Profile in Laminar and Turbulent Rectangular Jets. Major Professor: Huidan (Whitney) Yu.

We numerically investigate the underlying physics of two peculiar phenomena, which are axis-switching and saddle-back velocity profile, in both laminar and turbulent rectangular jets using lattice Boltzmann method (LBM). Previously developed computation protocols based on single-relaxation-time (SRT) and multiple-relaxation-time (MRT) lattice Boltzmann equations are utilized to perform direct numerical simulation (DNS) and large eddy simulation (LES) respectively.

In the first study, we systematically study the axis-switching behavior in low aspect-ratio (AR), defined as the ratio of width over height, laminar rectangular jets with $AR = 1$ (square jet), 1.5, 2, 2.5, and 3. Focuses are on various flow properties on transverse planes downstream to investigate the correlation between the streamwise velocity and secondary flow. Three distinct regions of jet development are identified in all the five jets. The 45° and 90° axis-switching occur in characteristic decay (CD) region consecutively at the early and late stage. The half-width contour (HWC) reveals that 45° axis-switching is mainly contributed by the corner effect, whereas the aspect-ratio (elliptic) feature affects the shape of the jet when 45° axis-switching occurs. The close examinations of flow pattern and vorticity contour, as well as the correlation between streamwise velocity and vorticity, indicate that 90° axis-switching results from boundary effect. Specific flow patterns for 45° and 90° axis-switching reveal the mechanism of the two types of axis-switching respectively.

In the second study we develop an algorithm to generate a turbulent velocity field for the boundary condition at jet inlet. The turbulent velocity field satisfies incompressible continuity equation with prescribed energy spectrum in wave space. Appli-

cation study of the turbulent velocity profile is on two turbulent jets with $Re = 25900$. In the jets with $AR = 1.5$, axis-switching phenomenon driven by the turbulent inlet velocity is more profound and in better agreement with experimental examination over the laminar counterpart. Characteristic jet development driven by both laminar and turbulent inlet velocity profile in square jet ($AR = 1$) is also examined. Overall agreement of selected jet features is good, while quantitative match for the turbulence intensity profiles is yet to be obtained in future study.

In the third study, we analyze the saddle-back velocity profile phenomenon in turbulent rectangular jets with AR ranging from 2 to 6 driven by the developed turbulent inlet velocity profiles with different turbulence intensity (I). Saddle-back velocity profile is observed in all jets. It has been noted that the saddle-back's peak velocities are resulted from the local minimum mixing intensity. Peak-center difference Δ_{pc} and profound saddle-back (PSB) range are defined to quantify the saddle-back level and the effects of AR and I on saddle-back profile. It is found that saddle-back is more profound with larger AR or slimmer rectangular jets, while its relation with I is to be further determined.

1. INTRODUCTION

A jet refers to a fluid flow issuing from a slot or nozzle, where a stream of fluid mixes with the surrounding medium. As a jet penetrates downstream, the entrainment at the interface between the fluid and surrounding medium leads the jet to expand radially. Depending on the structures and shapes of the slot, the flow field of the jet presents a variety of characteristics, which are of importance in engineering design and innovations.

1.1 Background and Research Motivation

Physical study of different types of jet has resulted in a number of practical applications. Fig. 1.1 shows a few examples: (a) A jet engine works by means of the propulsive force produced by the high-speed exhaust jet; the mixing performance between air jet and injected fuel in the combustion chamber affects how fast the exit stream can be. (b) The inkjet printer , as told by the name, is an invention utilizing jet on printing. (c) Hydraulic mining has been a fashion for mining gold and coal since over a century ago. In the picture, a mining worker is directing a high-pressure water jet to remove rock material and sediment from the desired composition. (d) Chemical-laser-weapon is an example of jet's application to military affairs.

Compared to traditional round jets, non-circular jets attract special attentions due to their enhanced entrainment and mixing properties, relative to those of comparable axisymmetric jets (Ref. [1] and references therein). Circular jets lack the corner vortex feature of square jets and aspect-ratio feature of elliptic jets, whereas rectangular jets combine both of these features. Hence we are more interested in the study of rectangular jet characteristics.

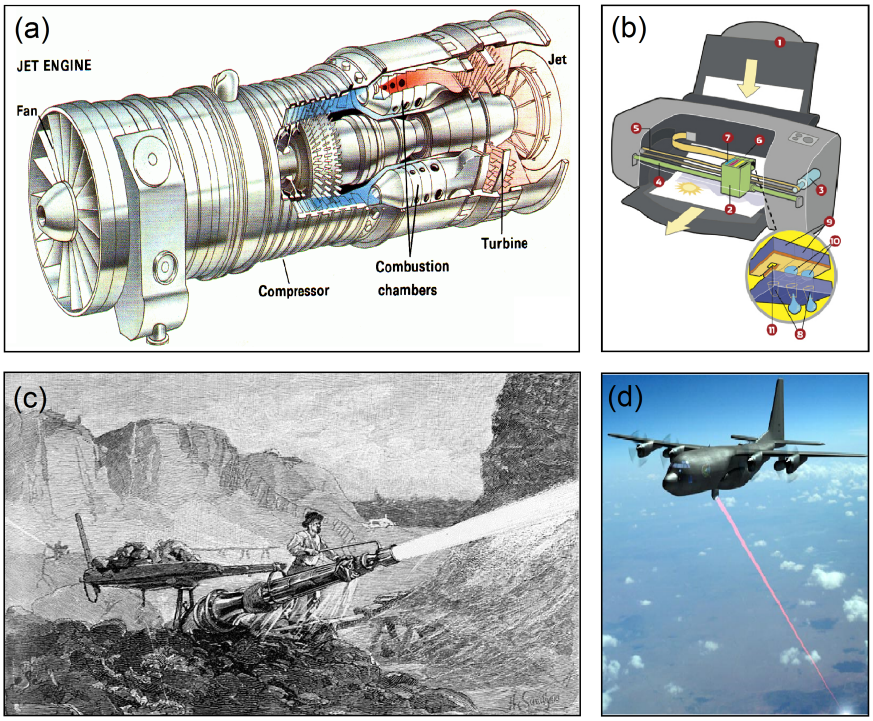

Figure 1.1. Representative jet applications: (a) jet engine, (b) inkjet printer, (c) hydraulic mining, (d) chemical laser. Figures are obtained from Internet.

Two peculiar behaviors of rectangular jets have been observed in experiments and computations [2–4]. Depending on initial conditions at the jet inlet, the cross-section of non-circular jets can evolve downstream through shapes similar to that at the jet inlet with its major and minor axis rotated at angles characteristic of the jet geometry. This phenomenon is called axis-switching. It has been known that axis-switching typically occurs in low aspect-ratio jets [4–8]. Another intriguing behavior is the development of a saddle-back velocity profile along major axis as the jet goes downstream. Fig. 1.2a shows the axis-switching phenomenon occurring in a triangular jet study [1], and Fig. 1.2a illustrates the saddle-back velocity profile observed in a rectangular jet study [4].

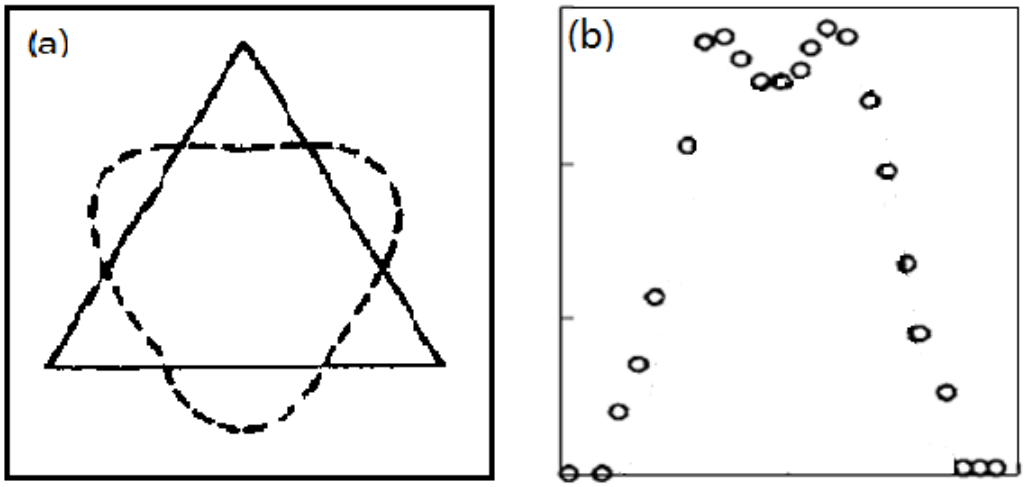

Figure 1.2. Characteristic jet behaviors: (a) jet cross-sections (solid line: initial shape, dashed line: current shape), representing axis-switching [1]; (b) saddle-back velocity profile [4].

In this thesis, we numerically investigate the underlying physics of two peculiar phenomenon, which are axis-switching and saddle-back velocity profile, in both laminar and turbulent rectangular jets using lattice Boltzmann method (LBM). Previously developed computation protocols solving single-relaxation-time and multiple-relaxation-time lattice Boltzmann equations are utilized to perform direct numerical and large eddy simulation for laminar and turbulent jets respectively.

In the first study, we systematically study the axis-switching behavior in low aspect-ratio (AR), defined as the ratio of width over height, laminar rectangular jets with $AR = 1$ (square jet), 1.5, 2, 2.5, and 3. Focuses are on various flow properties on transverse planes downstream to investigate the correlation between the streamwise velocity and secondary flow. Three distinct regions of jet development are identified in all the five jets. The 45° and 90° axis-switching occur in characteristic decay (CD) region consecutively at the early and late stage. The half-width contour (HWC) reveals that 45° axis-switching is mainly contributed by the corner effect, whereas the aspect-ratio (elliptic) feature affects the shape of the jet when 45° axis-switching occurs. The close examinations of flow pattern and vorticity contour, as well as the

correlation between streamwise velocity and vorticity, indicate that 90° axis-switching results from boundary effect. Specific flow patterns for 45° and 90° axis-switching reveal the mechanism of the two types of axis-switching respectively.

In the second study we develop an algorithm to generate a turbulent velocity field for the boundary condition at jet inlet. The turbulent velocity field satisfies incompressible continuity equation with prescribed energy spectrum in wave space. Application study of the turbulent velocity profile is on two turbulent jets with $Re = 25900$. In the jets with $AR = 1.5$, axis-switching phenomenon driven by the turbulent inlet velocity is more profound and in better agreement with experimental examination over the laminar counterpart. Characteristic jet development driven by both laminar and turbulent inlet velocity profile in square jet ($AR = 1$) is also examined. Overall agreement of selected jet features is good, while quantitative match for the turbulence intensity profiles is yet to be obtained in future study.

In the third study, we analyze the saddle-back velocity profile phenomenon in turbulent rectangular jets with AR ranging from 2 to 6 driven by the developed turbulent inlet velocity profiles with different turbulence intensity (I). Saddle-back velocity profile is observed in all jets. It has been noted that the saddle-back's peak velocities are resulted from the local minimum mixing intensity. Peak-center difference Δ_{pc} and profound saddle-back (PSB) range are defined to quantify the saddle-back level and the effects of AR and I on saddle-back profile. It is found that saddle-back is more profound with larger AR or slimmer rectangular jets, while its relation with I is to be further determined.

1.2 Lattice Boltzmann Method for Rectangular Jets

Lattice Boltzmann method (LBM) has emerged as an alternative model to simulate complex flows [5, 9]. Conventionally, computational fluid dynamics (CFD) solves Navier-Stokes equations on macroscopic level, whereas LBM solves Boltzmann equation on mesoscopic level [10]. The idea of LBM is that the collective behavior of many

microscopic particles result in the macroscopic dynamics of the flow. Thus, it has been well-known that LBM has physical and computational advantages over macroscopic CFD approaches due to its kinetic nature. Two of the most profound advantages are easy implementation of complex boundary conditions and parallelization of algorithm. LBM is also regarded as an ideal tool for GPU parallel computation. These advantages make LBM a rather promising alternative CFD method in the future.

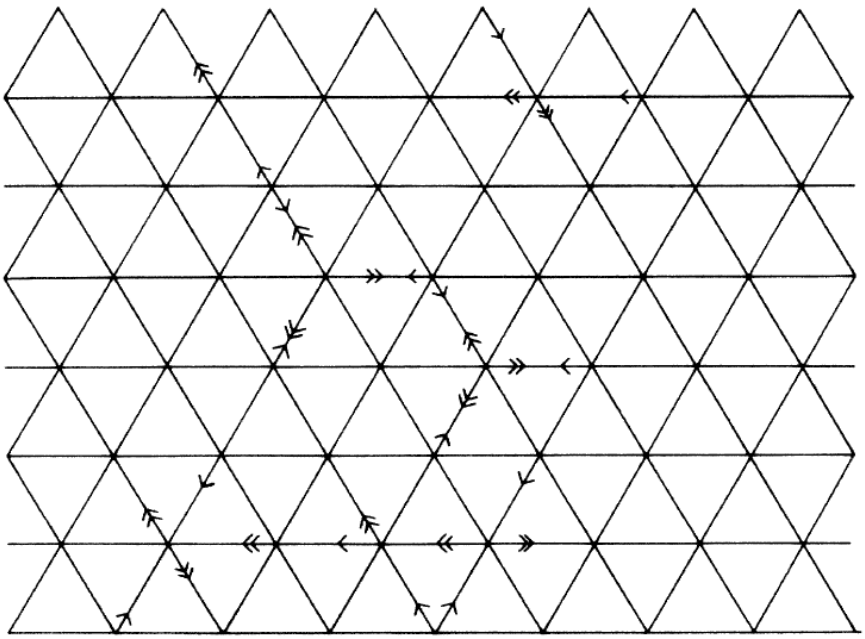

Figure 1.3. Lattice gas automata (LGA): triangular lattice with hexagonal symmetry and hexagonal lattice rules. Particles at time t and t+1 are marked by single and double arrows, respectively. Figure is obtained from [11].

LBM originated from lattice gas automata (LGA) [11] (Fig. 1.3), a model focusing on molecular kinetics in a discrete lattice and discrete time. LGA describes the status of each molecule on the nodes. The evolution equation of LGA, which conveys the basic concept of LBM, is as follows:

$$n_i(\boldsymbol{r} + \boldsymbol{e}_i, t+1) = n_i(\boldsymbol{r}, t) + \Omega_i(n(\boldsymbol{r}, t)), i = 0, 1, ..., M_n - 1 \tag{1.1}$$

where n_i denotes Boolean variables, describing the particle occupation on the grids, $\boldsymbol{e}_i$ are the molecular velocities and M_n stands for the number of directions for particle velocities; $\boldsymbol{r}$ and t are used to represent the current location and time step the particle is at. Two sub-steps are involved in the evolution of the status of each particle for each time step: (a) collision that is reflected by Ω_i, in which a particle getting to a node and change its velocities according to certain rules, and (b) streaming, when the particle moves to the adjacent grid directed by its velocity. The macroscopic variables at each grid are recovered by the collective information of the molecule:

$$\rho = \sum_i n_i, \rho \boldsymbol{u} = \sum_i n_i \boldsymbol{e}_i. \tag{1.2}$$

However, LGA suffers from statistical noise due to the non-linearity of the governing equations and unphysical hydrodynamical quantities resulted from velocity-dependent pressure [12].

LBM scheme was developed to overcome the aforementioned drawbacks. Instead of dealing with Boolean variables in LGA model, LBM manipulates distribution functions f_i, a set of variables that measure the possibilities of a particle migrating along finite discretized directions. A typical lattice Boltzmann equation looks like [12]

$$f_i(\boldsymbol{r} + \boldsymbol{e}_i \delta_t, t + \delta_t) = f_i(\boldsymbol{r}, t) - \frac{1}{\tau}[f_i(\boldsymbol{r}, t) - f_i^{(eq)}(\boldsymbol{r}, t)], i = 0, 1, ..., M_f - 1 \tag{1.3}$$

where f_i and $f_i^{(eq)}$ represent the M_f distribution functions and their equilibria, respectively; δ_t is the discrete time-step; τ is the relaxation time. The equilibrium distribution function $f_i^{(eq)}$ is expressed as

$$f_i^{(eq)} = \omega_i \rho \big[1 + \frac{3\boldsymbol{e}_i \cdot \boldsymbol{u}}{c^2} + \frac{9(\boldsymbol{e}_i \cdot \boldsymbol{u})^2}{2c^4} - \frac{3u^2}{2c^2}\big], i = 0, 1, ..., M_f - 1 \tag{1.4}$$

where ω_i denotes the weighting factors of the lattice, ρ, $\boldsymbol{u}$ and u are the density, velocity and its magnitude of the fluid, and $c \equiv \delta_x/\delta_t$, δ_x being lattice length. Density and momentum are obtained from the distribution functions as

$$\delta\rho = \sum_i f_i, \rho_0 \boldsymbol{u} = \sum_i \boldsymbol{e}_i f_i. \tag{1.5}$$

The fluid property and particle's collective behavior have the following relation:

$$\nu = \frac{1}{3}\left(\tau - \frac{1}{2}\right)c\delta_x. \tag{1.6}$$

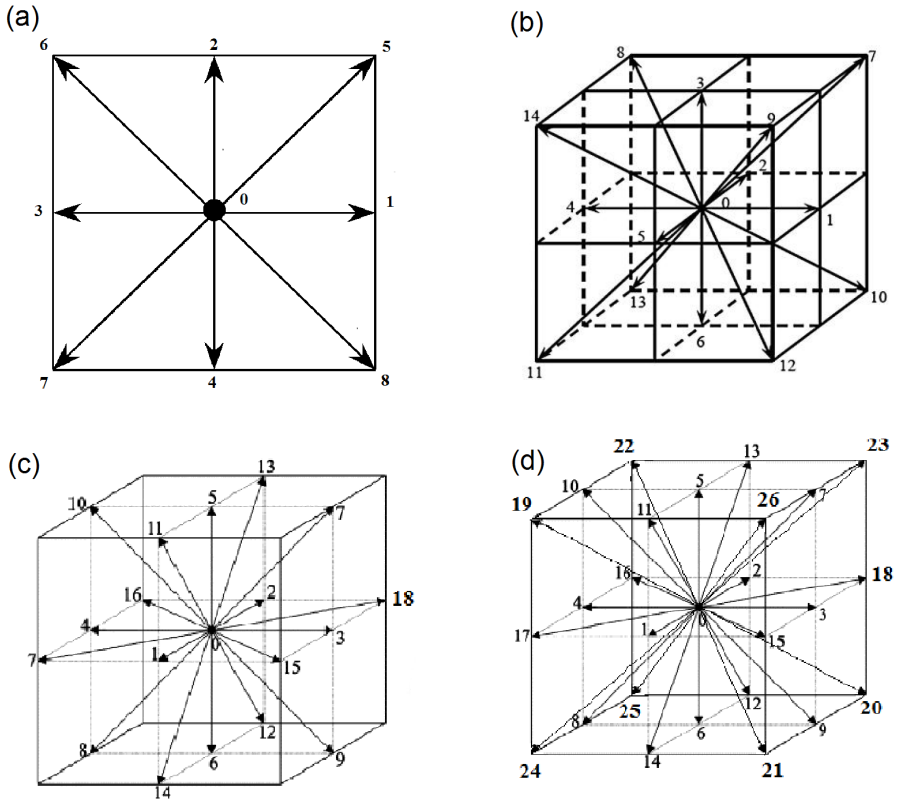

Figure 1.4. LBM lattice models: (a) D2Q9, (b) D3Q15, (c) D3Q19, (c) D3Q27. D: dimension, Q: number of discrete directions.

The implementation of LBM involves space and time discretization on the predefined lattice. Since the first validated hexagonal lattice, a variety of lattice models have been analyzed. Fig. 1.4 shows four prevailing lattice models in 2D (a) and

3D ((b)-(d)). The corresponding particle velocities and weighting factors are written below. D2Q9:

$$\boldsymbol{e}_i = \begin{cases} (0,0), & i = 0 \\ (\pm 1, 0), (0, \pm 1), & i = 1 \sim 4 \\ (\pm 1, \pm 1), & i = 5 \sim 8, \end{cases} \tag{1.7}$$

and

$$\omega_i = \begin{cases} \frac{4}{9}, & i = 0 \\ \frac{1}{9}, & i = 1 \sim 4 \\ \frac{1}{36}, & i = 5 \sim 8. \end{cases} \tag{1.8}$$

D3Q15:

$$\boldsymbol{e}_i = \begin{cases} (0,0,0), & i = 0 \\ (\pm 1, 0, 0), (0, \pm 1, 0), (0, 0, \pm 1), & i = 1 \sim 6 \\ (\pm 1, \pm 1, \pm 1), & i = 7 \sim 14, \end{cases} \tag{1.9}$$

and

$$\omega_i = \begin{cases} \frac{2}{9}, & i = 0 \\ \frac{1}{9}, & i = 1 \sim 6 \\ \frac{1}{72}, & i = 7 \sim 14. \end{cases} \tag{1.10}$$

D3Q19:

$$\boldsymbol{e}_i = \begin{cases} (0,0,0), & i = 0 \\ (\pm 1, 0, 0), (0, \pm 1, 0), (0, 0, \pm 1), & i = 1 \sim 6 \\ (\pm 1, \pm 1, 0), (\pm 1, 0, \pm 1), (0, \pm 1, \pm 1), & i = 7 \sim 18, \end{cases} \tag{1.11}$$

and

$$\omega_i = \begin{cases} \frac{1}{3}, & i = 0 \\ \frac{1}{18}, & i = 1 \sim 6 \\ \frac{1}{36}, & i = 7 \sim 18. \end{cases} \tag{1.12}$$

D3Q27:

$$\boldsymbol{e}_i = \begin{cases} (0,0,0), & i = 0 \\ (\pm 1,0,0),(0,\pm 1,0),(0,0,\pm 1), & i = 1 \sim 6 \\ (\pm 1,\pm 1,0),(\pm 1,0,\pm 1),(0,\pm 1,\pm 1), & i = 7 \sim 18, \\ (\pm 1,\pm 1,\pm 1), & i = 19 \sim 26, \end{cases} \tag{1.13}$$

and

$$\omega_i = \begin{cases} \frac{8}{27}, & i = 0 \\ \frac{2}{27}, & i = 1 \sim 6 \\ \frac{1}{54}, & i = 7 \sim 18, \\ \frac{1}{216}, & i = 19 \sim 26. \end{cases} \tag{1.14}$$

1.2.1 Single-relaxation-time Model

There are two prevailing lattice Boltzmann models. The single-relaxation-time model was directly developed from LGA [11], where a single relaxation time τ connects the collective behavior of molecules to kinematic viscosity of the fluid, as seen in Eq. 1.18. Here we express these models with an improved format [10]:

$$f_i^{(eq)} = \omega_i \left\{ \delta\rho + \rho_0 \Big[\frac{3\boldsymbol{e}_i \cdot \boldsymbol{u}}{c^2} + \frac{9(\boldsymbol{e}_i \cdot \boldsymbol{u})^2}{2c^4} - \frac{3u^2}{2c^2} \Big] \right\} \tag{1.15}$$

where $\delta\rho$ is the density fluctuation and ρ_0 is the constant mean density of the system. In LBM the values of ρ_0, δ_x, and δ_t are all typically set to unity. The sound speed in this model is $c_s = c/\sqrt{3}$. The total density is $\rho = \rho_0 + \delta\rho$. The mass and momentum conservations are strictly enforced:

$$\delta\rho = \sum_i f_i = \sum_i f_i^{(eq)} \tag{1.16}$$

$$\rho_0 \boldsymbol{u} = \sum_i \boldsymbol{e}_i f_i = \sum_i \boldsymbol{e}_i f_i^{(eq)} \tag{1.17}$$

The fluid kinematic viscosity ν has the following relation with the relaxation time τ:

$$\nu = \frac{1}{3}\Big(\tau - \frac{1}{2}\Big) c\delta_x, \tau = \frac{3\nu}{c\delta_x} + \frac{1}{2} \tag{1.18}$$

1.2.2 Multiple-relaxation-time Model

The multiple-relaxation-time (MRT) model is more sophisticated [5]. Instead of one single relaxation time, MRT has a number of relaxation times to fluid properties. It also consists of collision and streaming for tackling particle's relaxation and advection respectively. The major advantage of MRT over SRT includes the possibility to rapidly dissipate non-hydrodynamic moments and suppress non-physical small-scale oscillations quickly [5], when appropriate relaxation times are selected. Meanwhile, MRT model achieves better numerical stability [13] and higher accuracy of boundary implementation [14].

The MRT lattice Boltzmann equation reads

$$|f(\boldsymbol{r}+\boldsymbol{e}_i\delta_t, t+\delta_t)\rangle - |f(\boldsymbol{r},t)\rangle = -M^{-1}\hat{S}[|m(\boldsymbol{r},t)\rangle - |m^{(eq)}\times(\boldsymbol{r},t)\rangle], \tag{1.19}$$

where $|\rangle$ represents the Dirac notation for vectors, i.e., $|f(\boldsymbol{r}+\boldsymbol{e}_i\delta_t, t+\delta_t)\rangle \equiv [f_0(\boldsymbol{r}+\boldsymbol{e}_i\delta_t, t+\delta_t), f_1(\boldsymbol{r}+\boldsymbol{e}_i\delta_t, t+\delta_t), ..., f_{18}(\boldsymbol{r}+\boldsymbol{e}_i\delta_t, t+\delta_t)]^T$. And we use $|m\rangle$ and $|m^{(eq)}\rangle$ to represent the moment components of $|f\rangle$ and their equilibria. $\hat{S}$, called diagonal collision matrix, is defined as

$$\hat{S} \equiv diag(0, s_1, s_2, 0, s_4, 0, s_4, s_4, s_9, s_2, s_9, s_2, s_9, s_9, s_9, s_{16}, s_{16}, s_{16}), \tag{1.20}$$

where s_i $(i = 1, 2, 4, 9, 16)$ are parameters related to the different relaxation time scales applied. In MRT model, distribution functions and corresponding momenta are related by a transformation matrix M in the following fashion: $|m\rangle = M|f\rangle$ or $|f\rangle = M^{-1}|m\rangle$. How to calculate $|m^{(eq)}\rangle$ can be found in [15], as well as the values of M and $\hat{S}$ for our D3Q19 lattice model. There is slight variation in calculating kinematic viscosity ν compared to the SRT model (Eq. 1.18):

$$\nu = \frac{1}{3}(\frac{1}{s_9} - \frac{1}{2})c\delta_X \tag{1.21}$$

and

$$s_9 = \frac{2c\delta_X}{6\nu + c\delta_X}. \tag{1.22}$$

With MRT's another advantage, one can calculate the strain-rate from the non-equilibrium moments directly using the formula give below:

$$S_{\alpha\beta} = -\frac{1}{2\rho s_9 c_s^2} \sum_i \boldsymbol{e}_{i\alpha}\boldsymbol{e}_{i\beta}(f_i - f_i^{(eq)}), \alpha, \beta = 1, 2, 3, \tag{1.23}$$

where s_9 is computed in Eq. 1.22, and both α and β mean the corresponding component of $\boldsymbol{e}_i$.

1.2.3 Computation Set-up and Characteristic Regions of A Rectangular Jet

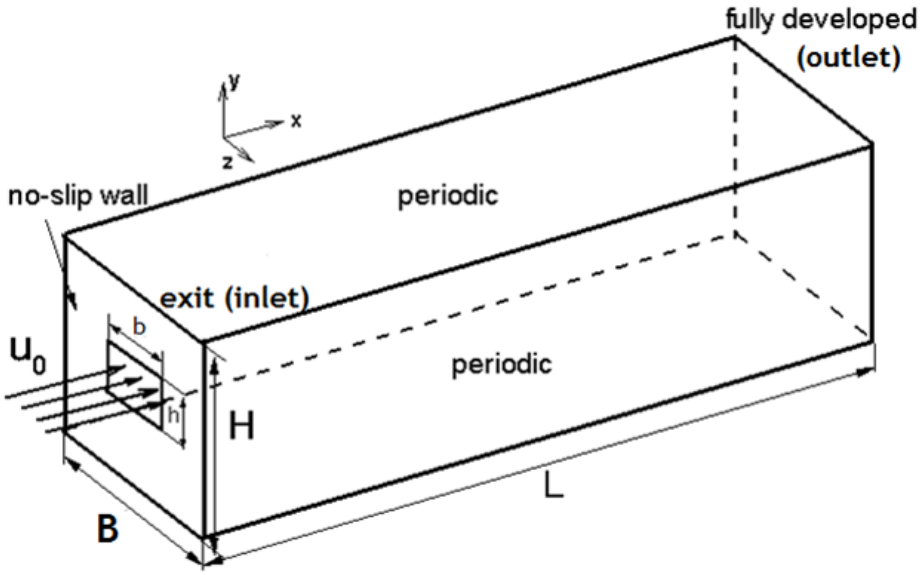

Figure 1.5. Schematic of the computation set-up.

The computation set-up for a rectangular jet is shown in Fig. 1.5. The x, y, and z axes are parallel to streamwise, lateral and spanwise directions respectively. The whole domain is a $B \times H \times L$ channel. The flow issues with a uniform streamwise velocity $u = u_0$ ($v = w = 0$) from a $b \times h$ orifice slot located at the centre of the

plane ($x = 0$, $-b/2 \leq z \leq b/2$, and $-h/2 \leq y \leq h/2$). The jet orifice is simplified as a plane. We apply bounce-back boundary [16]

$$f_i^* = f_i - 6\omega_i \rho_0 \boldsymbol{u}_0 \cdot \boldsymbol{e}_i \tag{1.24}$$

at jet orifice plane ($x = 0$) where f_i^* is the distribution function of $\boldsymbol{e}_i^* = -\boldsymbol{e}_i$, fully developed boundary at outflow ($x = L$), and periodic boundary conditions in both spanwise and lateral directions. The detail description of the jet slot and corresponding flow field is show in Fig. 1.6.

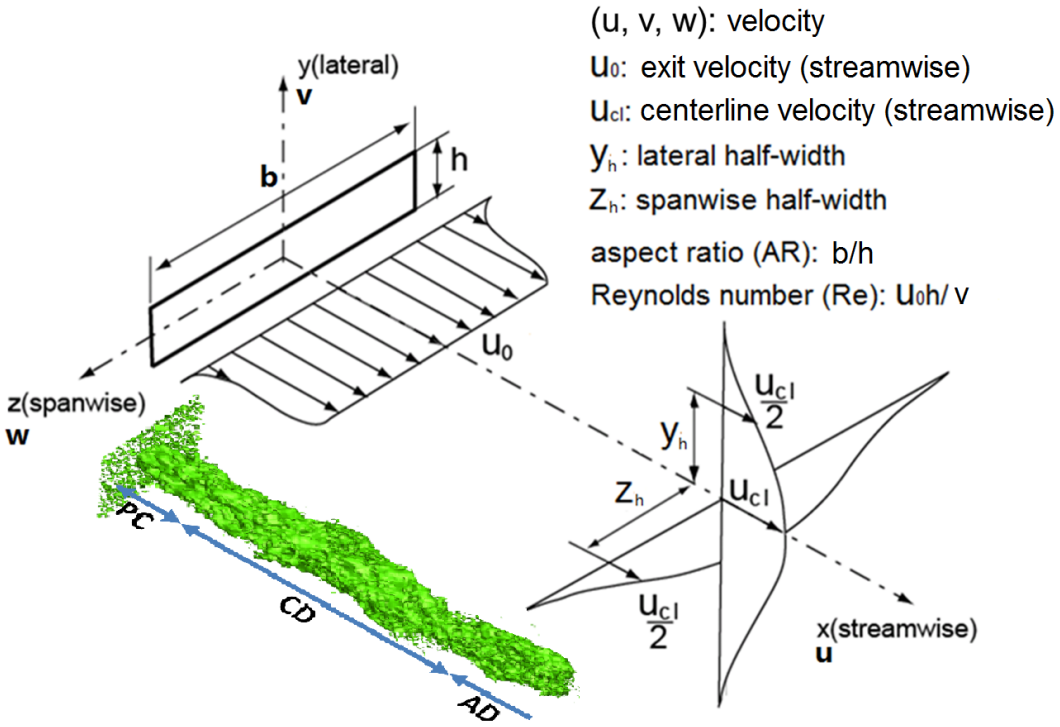

Figure 1.6. Illustrations of coordinate system, jet slot dimension, flow field and characteristic regions, copied from [5].

In Fig. 1.6. u, v and w represent streamwise, lateral and spanwise velocities respectively. Centerline velocity $u_{cl} = u(x, 0, 0)$ and lateral and spanwise half-widths (y_h, z_h) are determined by equations

$$u(x, y_h, 0) = u(x, 0, z_h) = \frac{1}{2} u_{cl}. \tag{1.25}$$

Aspect ratio (AR) of the jet is defined as the ratio of the width b over height h of the jet slot, while the Reynolds number (Re) is based on the lateral dimension h of the inlet, exit velocity u_0, and kinematic viscosity ν of the fluid.

Early experimental and analytical investigations [17–19] have revealed that fully developed flow field (in green, Fig. 1.6) of a rectangular jet is characterized by three distinct regions: (i) PC (potential core) region into which the mixing initiated at the jet boundaries has not penetrated; (ii) CD (characteristic decay) region where velocity decay and mixing depend on the jet aspect ratio and shape; (iii) AD (axisymmetric decay) region extending to infinity where the velocity field is axisymmetric independent of the jet inlet shape. These region divisions are roughly sketched out by the side of flow contour in Fig. 1.6.

2. MECHANISM OF AXIS-SWITCHING IN LAMINAR RECTANGULAR JETS

2.1 Description

Axis-switching, in the jet study, refers to the rotation of the jet's cross-section's axes as the jet develops. It has been a topic of interest for over last few decades, for the insight it provides in understanding fundamental physics and developing practical applications. Axis-switching phenomenon has been observed for a variety of jet scenarios since more than three decades ago, including elliptic jets [2, 20–30], rectangular jets [3–8,31,32], and jets with more complicated geometry [1,33–35]. It has been believed that in elliptic jets, the underlying mechanism of axis-switching behavior results from self-induced Biot–Savart deformation of vortex rings due to non-uniform azimuthal curvature and interaction between azimuthal and streamwise vorticities [1]. Not too long ago, an experiment confirmed the azimuthal vortex deformation in the region of the axis-switching of a lobed orifice jet [36].

Rectangular jets combine the variable-aspect-ratio feature of elliptic jet with the corner vortex feature of square jets. This combination yields features which do not appear in elliptic jets and are of importance in practical applications. One example is the axis-switching of 45° in a square jet $AR = 1$ and 90° in rectangular jet $AR = 1.5$ [3].

In this chapter we want to investigate axis-switching in rectangular jets by systemically studying one square jet and four rectangular laminar jets at a relatively low Reynolds number listed in Table 2.1, through direct numerical simulation (DNS) using LBM. Focus is on the correlations between the primary downstream penetrating flow and the secondary entertainment on transverse planes to reveal the mechanism of axis-switching in rectangular jets.

Table 2.1. Five jets conducted in this study. The unit for length is meter(m).

Jet	AR	b, h	B, H, L	jet grid size	Domain grid size
I	1	$0.01, 0.01$	$0.063, 0.063, 1.0$	$8, 8$	$50, 50, 800$
II	1.5	$0.015, 0.01$	$0.063, 0.063, 1.0$	$12, 8$	$50, 50, 800$
III	2	$0.02, 0.01$	$0.063, 0.063, 1.0$	$16, 8$	$50, 50, 800$
IV	2.5	$0.025, 0.01$	$0.063, 0.063, 1.0$	$20, 8$	$50, 50, 800$
V	3	$0.03, 0.01$	$0.063, 0.063, 1.26$	$24, 8$	$50, 50, 1000$

For the simplicity of implementation, we employ D3Q19 SRT lattice model for the laminar jet simulations. Besides, for a relatively low Reynolds number, DNS is applied for the advantage of high accuracy without sacrificing much computation cost. In this lattice model, the 3D discrete phase space is defined by cubic lattice with 19 discrete particle velocities by Eq. 1.11 and weighting factors by Eq. 1.12.

For the remainder of this chapter, we show results on the mechanism of 45° and 90° axis-switching through the correlations between the primary downstream velocity and the vorticity on transverse planes before concluding the axis-switching study with a short discussion.

2.2 Results

2.2.1 Characteristic Regions

For the given dimension of the jets, we first identify the three characteristic regions for each jet at a representative Reynolds number ($Re = 200$) with $u_0 = 23(m/s)$ and $\nu = 1.51e - 5(m^2/s)$ in Table 2.2 through monitoring the shape of jet through the half-width contour (HWC) on each transverse planes at each downstream grid. The

HWC on an x-plane is the contour of the grid points ($y_{\frac{1}{2}}$, $z_{\frac{1}{2}}$) where the streamwise velocity is half of the centerline velocity:

$$u(x, y_{\frac{1}{2}}, z_{\frac{1}{2}}) = \frac{1}{2} u_{cl} \tag{2.1}$$

The onset of the CD region is determined when the original lines and corners of the rectangular or square shape of the HWC become round, whereas the onset of the AC region is where the shape of the HWC becomes circular. It shows that the length of PC region is independent of the jet AR when normalized by h, whereas the range of CD region varies with AR. Bigger AR corresponds to longer CD region. When AR changes from 1 to 3, the length of CD region varies with different AR. The bigger the AR, the longer the length of the CD region. When AR changes from 1 to 3, the length of the CD region doubles.

Table 2.2. Lengths of PC, CD regions for different AR at $Re = 200$.

Jet	AR	PC	CD	AD
I	1	x$\leq$ 0.38h	0.38h $<$ x $\leq$ 37h	x $>$ 37h
II	1.5	x $\leq$ 0.75h	0.75h $<$ x $\leq$ 57h	x $>$ 57h
III	2	x $\leq$ 0.75h	0.75h $<$ x $\leq$ 64h	x $>$ 64h
IV	2.5	x $\leq$ 0.75h	0.75h $<$ x $\leq$ 74h	x $>$ 74h
V	3	x $\leq$ 0.75h	0.75h $<$ x $\leq$ 82h	x $>$ 82h

2.2.2 45° and 90° Axis-switching

The HWC is a direct measure of the level of jet mixing. Fast spreading of HWC indicates rapid entrainment and mixing. The physics of entrainment and HWC evolution can be understood by examining the secondary flow: i.e., flow on the transverse plane (y, z) normal to the primary flow direction (x). Figure 2.1 shows the downstream evaluation of HWC at $Re = 200$ for jet (a) I,(b) II,(c) III, and (d) V at

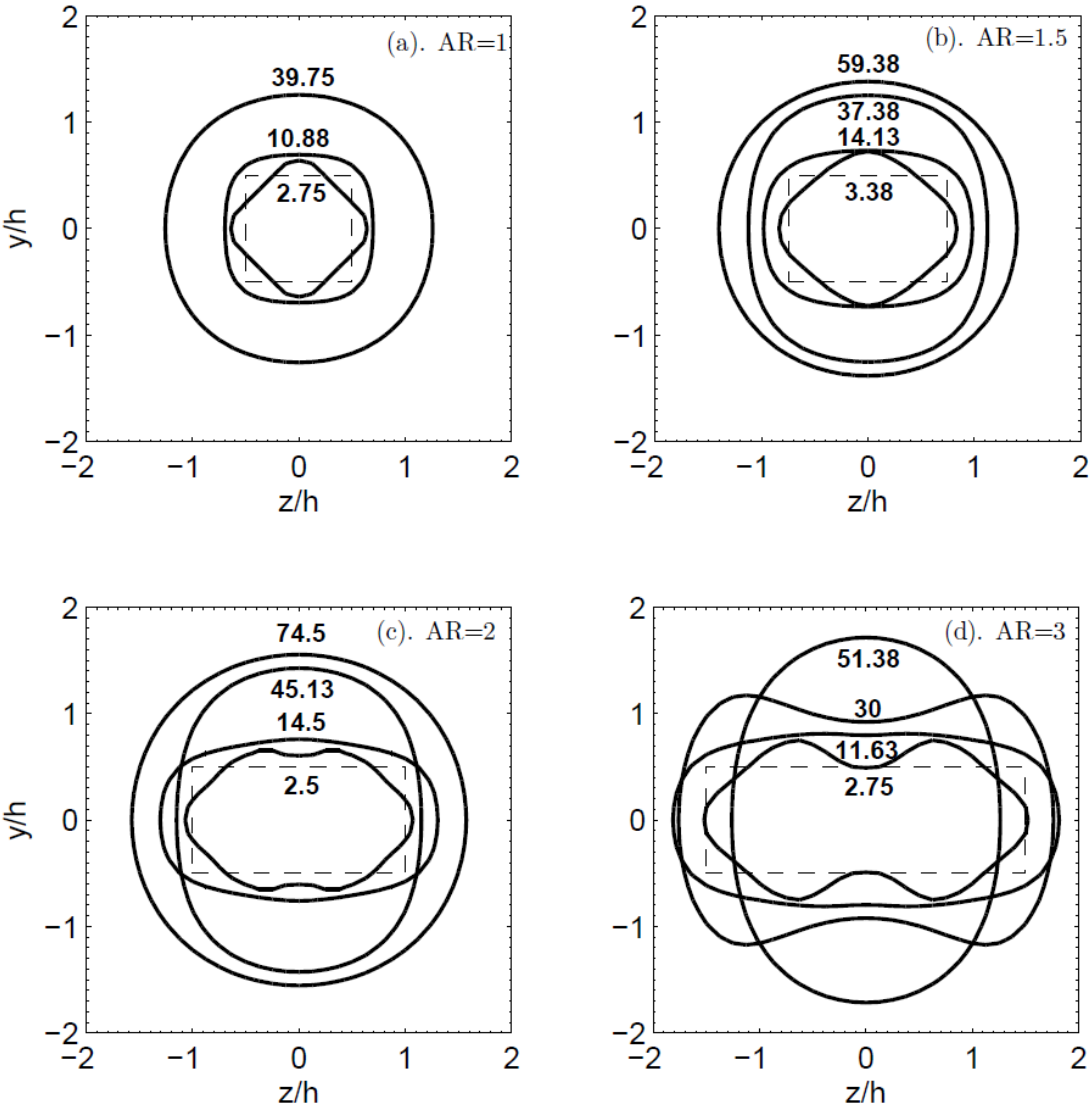

Figure 2.1. Downstream evaluations of HWC of jet (a) I,(b) II,(c) III,(d) V at indicated representative downstream locations, Re = 200.

representative downstream locations. The numbers adjacent to the HWC lines in the figures are the downstream distance from the jet inlet normalized by the jet inlet height h. In the square jet (Fig. 2.1 (a)), the jet starts from a square (dashed

line) shape. The axes switch 45° at $x = 2.75h$,and then switch back to a round square shape at $x = 10.88h$. At location $x = 39.75h$, the jet becomes axisymmetric, indicating that the AD region starts. As speculated, the AD region extends to infinity. The axis-switching in rectangular jets are more interesting since there will be two axis-switchings occurring downstream as shown in Fig. 2.1 (b)-(c). For example, jet II ($AR = 1.5$) starts from a rectangular shape (dashed line) at the jet inlet, first switches 45° at $x = 3.38h$, then switches back as a rounded rectangle at $x = 14.13h$, then switches again to 90° at $x = 37.38h$, and eventually becomes round at $x = 59.38h$. The features of axis-switching in rectangular jets may be summarized as follows.

- 45° axis-switching occurs in all five rectangular jets at approximately the same downstream location independent of AR, implying that the 45° axis-switching results in the corner vortex feature unique in rectangular jets.

- The shape of jet when 45° axis-switching occurs varies from a diamond ($AR = 1$), to rhombus ($AR = 1.5$), to deformed rhombuses with saddle-back around the center of the minor axis ($AR \geq 2$), indicating that the aspect ratio does affect the jet entrainment to the surrounding, which is a feature of elliptic jets. Thus, the axis-switchings in a rectangular jet are contributed by both corner effect and aspect-ratio effect.

- 90° axis-switching follows 45° axis-switching. A smaller-AR jet develops the 90° axis-switching closer to the jet inlet than a larger-AR jet.

- Both 45° and 90° axis-switching happen in CD region. The former is before the latter, implying that the corner feature is kicked in early then the elliptic feature.

- Dumbbell velocity contour observed in 45° axis-switching for relatively large-AR jets is another peculiar behavior in rectangular jets reported in experiments

[7, 8, 19, 37, 38] and computation [5], which will be a focus in our future study, thus not discussed here.

2.2.3 Velocity-Vorticity Correlation

Close look has been taken on the correlation of penetrating velocity u of primary flow and flow on transverse planes. Figures 2.2 show various properties including normalized downstream velocity (u/u_{cl}), downstream vorticity ($\omega_x = \frac{\partial w}{\partial y} - \frac{\partial v}{\partial z}$), secondary flow velocity ($\boldsymbol{V} = v\boldsymbol{j} + w\boldsymbol{k}$) and its magnitude ($V_m = \sqrt{v^2 + w^2}$) on representative downstream planes: (1) $x = 3.38h$; (2) $x = 14.13h$; (3) $x = 37.38h$; (4) $x = 59.38h$, corresponding to the contour lines in Fig. 2.1 (b) for jet II ($AR = 1.5$). The four representative downstream planes correspond to the typical stages of the jet development, 45° axis-switching, round rectangle, 90°, and circle as described above where only the half-velocity contour ($u/u_{cl} = 0.5$) lines are presented. From Fig. 2.2 (A), it is seen that axis-switchings, both 45° and 90°, occur on almost all the levels of u/u_{cl}. The 45° axis-switching (Fig. 2.2 (A) (1)) seems more significant when the velocity ratio reduces outward, whereas the 90° axis-switching (Fig. 2.2 (A) 3) is stronger when the velocity ratio is large. The corresponding vorticity contours, secondary vector fields and their magnitude contours are shown in Fig. 2.2 (B), (C), and (D). These patterns will be discussed later in this work.

Inspired by the fact that the secondary flow is induced due to the entrainment with the surroundings when the jet is penetrating downstream, we define the correlation function of penetrating velocity u and vorticity ω_x as

$$\rho_{u\omega} = \frac{\langle u(m,n)|\omega_x(m,n)|\rangle}{\sqrt{\langle u^2(m,n)\rangle\langle\omega_x^2(m,n)\rangle}} \tag{2.2}$$

where $\langle\cdots\rangle$ represents volume averaging for homogeneous turbulence and where summation over repeated indices is understood. Figure 2.3 shows the correlation functions of velocity and vorticity along downstream direction for the five jets. It is shown that velocity and vorticity quickly team up to a peak after the jet starts to develop. Close examination indicates that the 45° axis-switching occurs right after the peak in each

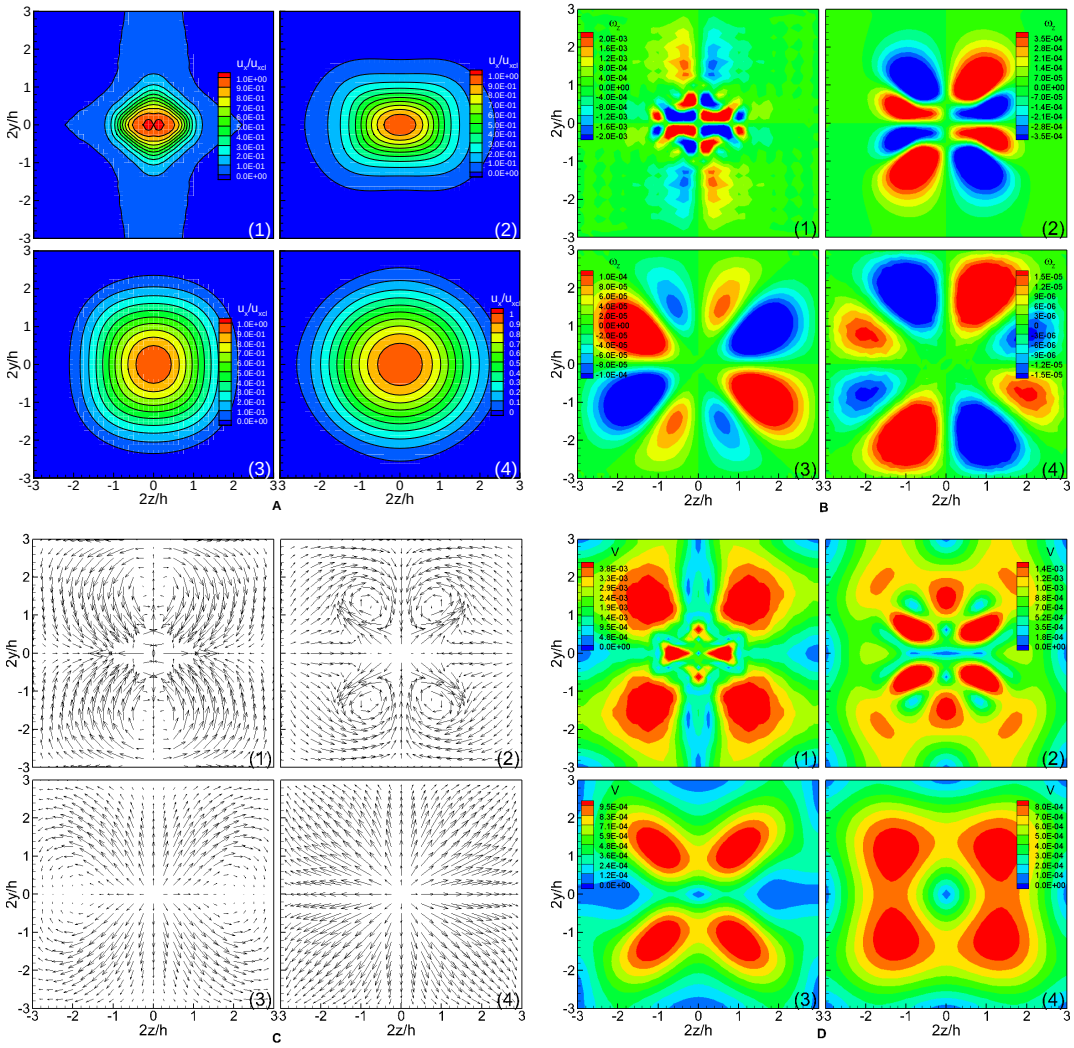

Figure 2.2. Secondary flow properties of jet with $AR = 1.5$ on representative downstream planes: (1) $x = 3.38h$; (2) $x = 14.13h$; (3) $x = 37.38h$; (4) $x = 59.38h$, corresponding to the contour lines in Fig. 2.1 (b). (A): contour fields of normalized penetrating velocity in the direction of jet propagates, u_x/u_{cl}; (B): contour fields of vorticity $\omega_x = \frac{\partial u_z}{\partial y} - \frac{\partial u_y}{\partial z}$; (C): vector fields of the secondary flow, $\boldsymbol{V} = u_y\boldsymbol{j} + u_z\boldsymbol{k}$; (D): contour fields of velocity magnitude of the secondary flow, $V = \sqrt{u_y^2 + u_z^2}$.

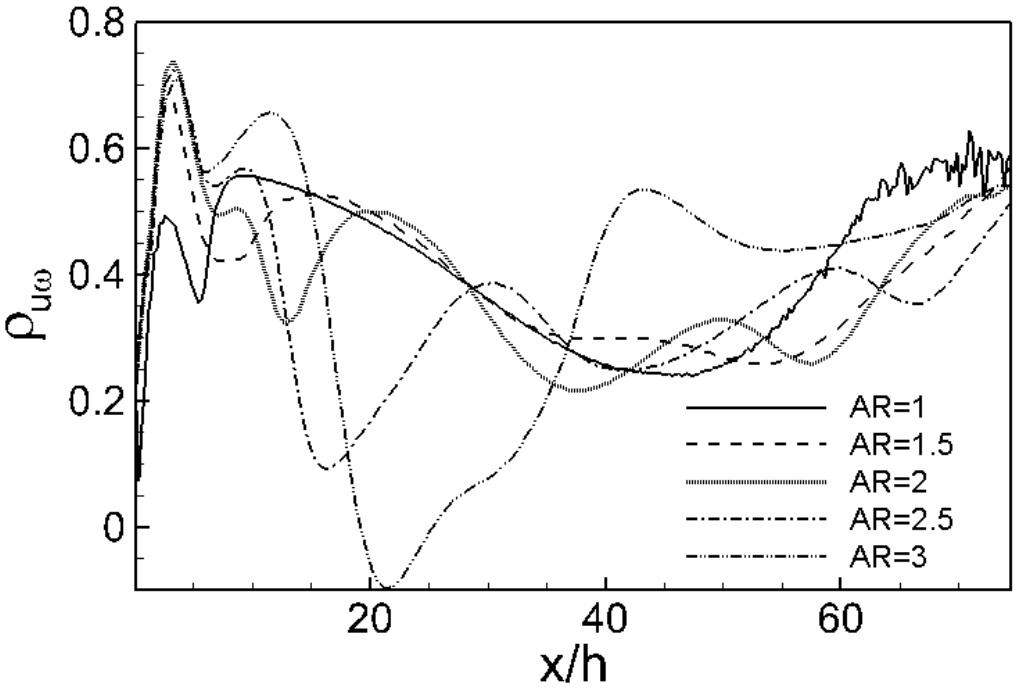

Figure 2.3. Correlation function of velocity and vorticity along downstream direction for the five jets. Solid line: $AR = 1$; dashed line: $AR = 1.5$; dotted line: $AR = 2$; dash-dot line: $AR = 2.5$; dash-dot-dot line: $AR = 3$.

jet. In the course to develop 90° axis-switching, the correlation function fluctuates quite a bit, shifting between coloration and decoloration and bigger AR jet tends to have bigger fractionation. At the late stage when the jet becomes circular, the correlation function tends to approach 0.5 and maintain.

2.2.4 Flow Pattern and Mechanism

We now reveal the underlying mechanism of axis-switching. Through close inspection of the secondary velocity field and vorticity on the transverse planes just before the axis-switching occurs, we are able to identify specific patterns for 45° and 90° axis-switching, shown in Figs. 2.4 and 2.5 respectively, which are considered as the triggers for the axis-switchings. In Fig. 2.4, it can be seen that the velocity at the

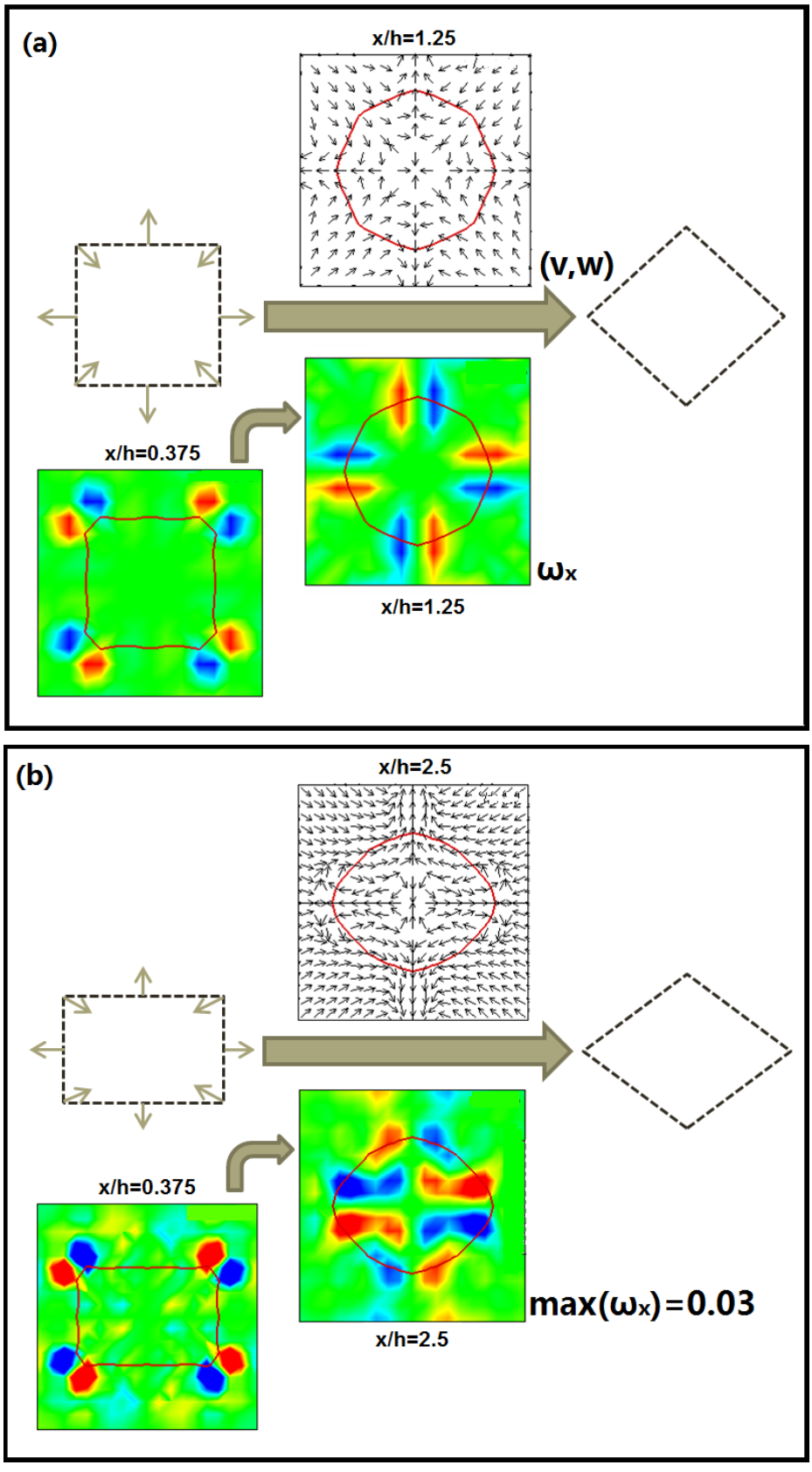

Figure 2.4. Flow pattern and vorticity field for 45° axis-switching. (a) Square jet; (b) Rectangular jet.

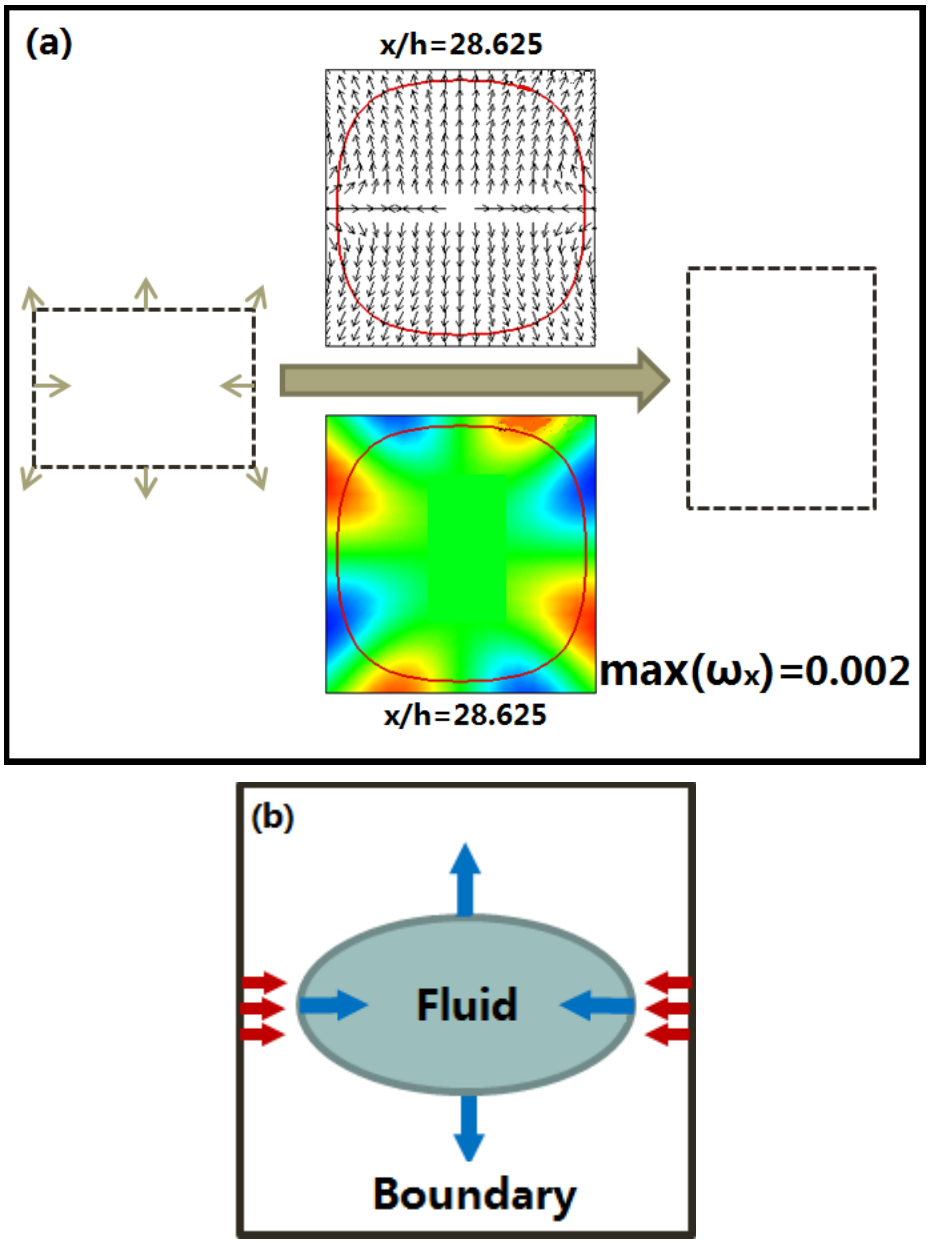

Figure 2.5. 90° axis-switching mechanism: (a) Flow pattern and vorticity field; (b) Boundary effect.

four corners of jet profile is uniformly toward the center while the flow is expanding outward at the four sides. Meanwhile, corresponding vorticity fields indicate that 45° axis-switching follows the occurrence of vortex pairs at the corners, which contribute a centripetal momentum and thus result in 45° axis-switching afterward. This mechanism applies to 45° axis-switching in both square and rectangular jets. The difference between 45° axis-switching in square (Fig. 2.4 (a)) and rectangular jet (Fig. 2.4 (b)) is that in the latter, the pair of vorticity along spanwise is stronger than that along lateral while both pairs are equally strong in the former. Similar approach is applied to shed some light on 90° axis-switching in rectangular jets. The 90° axis-switching is driven by a different pattern as shown in Fig. 2.5. There is strong inflow stream along spanwise and outflow stream along lateral, driving the jet to elongate in the lateral direction. The boundary effect is profound for 90° axis-switching. When the jet develops, the major direction approaches the boundary first and is squeezed by the boundary, leading the flows changes from the major to minor direction, to 90° axis-switching. The vorticity point of view is no more applicable since its magnitude has become very small (0.002 in LBM unit) in Fig. 2.5 (a) compared to 0.03 in Fig. 2.4 (b) to exert the influence on bringing about 90° axis-switching.

2.3 Conclusions and Discussion

Through SRT-DNS-LBM, we systematically studied axis-switching phenomena in five low aspect-ratio rectangular jets. Although the axis-switching in elliptic jet was extensively studied in the past, axis-switching behavior in rectangular jets is more complicated due to the fact that rectangular jets combine the variable aspect-ratio feature of elliptic jets with the corner vortex feature of square jets. The underlying fluid dynamical mechanism is far from clear. In this work, we focus on the correlation between downstream velocity and secondary flow. The development of the HWC lines clearly exhibit two consecutive axis-switchings when the jet is propagating, indicating richer mixing features than square or elliptic jets. The 45° axis-switching occurs

shortly after the jet enters the characteristic decay (CD) region while 90° appears when the jet is about to exit from the CD region toward the axisymmetric decay region. It is found that the location of 45° axis-switching has weak dependence of the jet AR yet the shape of the 45° axis-switching varies with AR, implying that the 45° axis-switching is contributed by both corner feature and elliptic feature. The 90° axis-switching seems to have a different story. As the jet develops, it spreads through the mixing and entrainment with the surroundings. When the flow in the major axis approaches the boundary, the entrainment in the major axis is weakened while the mixing along the minor axis becomes competitive to the major axis. As the jet further develops, the flow along minor axis exceeds that along the major axis, which is how the 90° axis-switching occurs. In our study, we synthesized two specific patterns to reveal the underlying dynamics from the secondary velocity field and vorticity contour to reveal the mechanism of the 45° and 90° axis-switching.

3. TURBULENT INLET VELOCITY PROFILE

3.1 Introduction

Turbulent rectangular jets were systemically studied in a previous work [5], using MRT-LBM. To achieve relatively high Reynolds numbers from 14,000 to 184,000, comparable to the experiments, large-eddy-simulation (LES) were performed. Extensive comparisons with experiment and computations to validate the MRT-LBM-lES approach. In spite of good overall agreements of mean field statistics such as normalized centerline velocity development and MSV profiles, the characteristics close to the inlet like turbulence intensity profiles, were not well captured. For example, certain degree of disagreement between simulation results and Quinn's experimental data [39] was seen in the matter of centerline mean streamwise velocity (MSV) decay and turbulence levels. This disagreement was attributed the fact that their simulation did not account for unsteady inflow condition as implemented in the experiment. In an attempt to confirm this concern and well capture the turbulence features of the turbulent rectangular jets, we develop and generate a turbulent inlet velocity profile, and re-simulate the turbulent jets.

Motivated by Petersen's Ph.D. dissertation [40], we consider the generation of turbulent inlet velocity profile as follows.

For a turbulent inlet, the two-dimensional (2D) velocity field consists of two parts, i.e.,

$$u_i = U_i + u_i', \tag{3.1}$$

where U_i accounts for the mean velocity distribution generally given, while u_i' is the mean-free fluctuation component which, combined with U_i, determines the field's turbulence intensity. After the decomposition of velocity, the generation of a turbulent inlet (u_i) goes down to that of s 2D fluctuating velocity field (u_i').

For incompressible flow, u_i' must satisfy continuity equation:

$$\frac{\partial u_i'}{\partial x_i} = 0. \tag{3.2}$$

Meanwhile, the fluctuation field is enforced with a prescribed energy spectrum, which makes it possible to adjust the motion scales of the turbulence injected. The intensity of turbulence in the velocity profile is easily adjustable by adding a factor to u_i'. In this way, comparisons can be made between jets with different energy spectra and turbulence intensity at the inlet, and their effects on the jet development is likely to be obtained.

3.2 Algorithm

The general idea is described as follows. First, we generate a three-dimensional (3D) isotropic fluctuating velocity field, which fulfils the continuity and specified energy spectrum mentioned above. Then we select a plane in the 3D space and extract its velocity distribution as the 2D u_i' to be applied in Eq. 3.1, by which the desired turbulent inlet u_i is obtained.

There are eight steps and to achieve such a turbulent inlet velocity profile, as illustrated in Fig 3.1. The procedures are implemented with coding work under the Matlab environment. All related functions are listed in the parentheses at the end of each step in the following paragraphs.

Step 1 initializes the fluctuating velocities $u_i'(n_1, n_2, n_3)$, $i = 1, 2, 3$, randomly in the physical space, with each component's magnitude ranging from -1 to 1. n_1, n_2 and n_3 are the coordinate indices of a component in the space along each axis. The dimensions of u_i', N_1, N_2, N_3, should be chosen so that two of them (say N_1 and N_2) match the grid size of the inlet of jet to be simulated, and the third one has to be large enough to get adequate variability. (**rand**)

Step 2 conducts a 3D fast Fourier transformation (FFT) with $u_i'(n_1, n_2, n_3)$ to get their spectral counterparts $\tilde{u_i'}(k_1, k_2, k_3)$. (**fftn**)

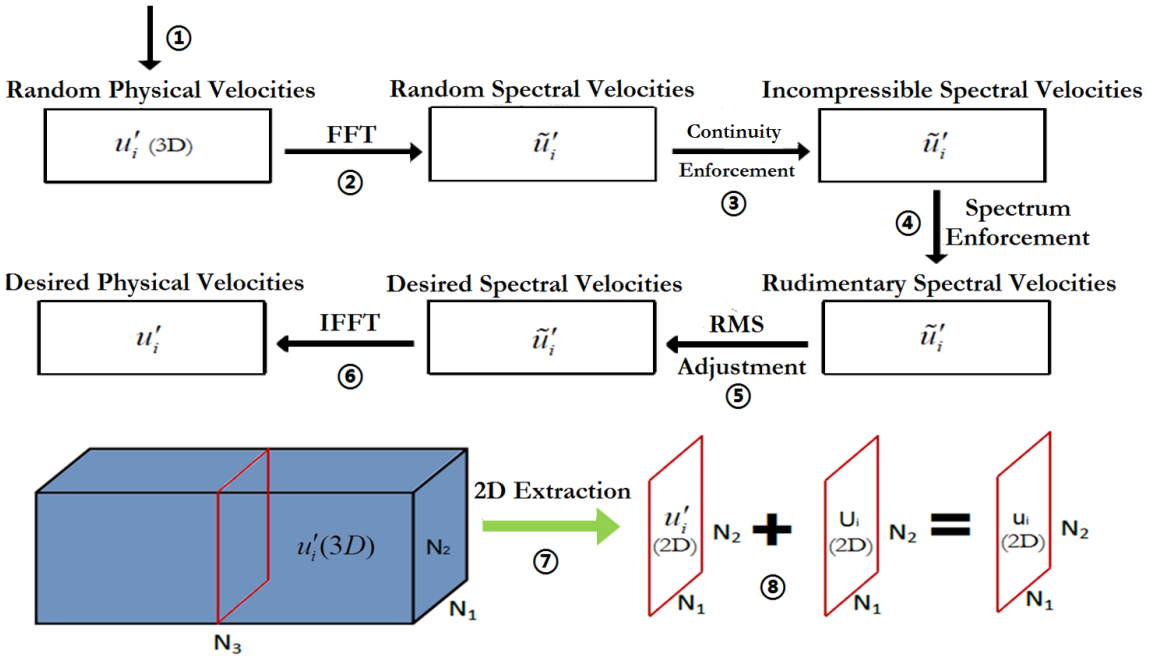

Figure 3.1. Flow chart for turbulent inlet velocity profile generation.

Here for an odd number of field dimension N_i, the wavenumber k_i and index n_i are related as

$$k_i(n_i) = \begin{cases} n_i - 1 & 1 \le n \le \frac{N_i+1}{2} \\ n_i - 1 - N_i & \frac{N_i+1}{2} \le n \le N_i. \end{cases} \tag{3.3}$$

Step 1 and 2 makes sure u_i' are real when $\tilde{u_i'}$ are transformed back into physical space in Step 7.

Step 3 applies the formula below to get a divergence-free velocity field for each velocity component to satisfy incompressibility. The enforcement of incompressibility is achieved by subtracting the dilatational part from the original velocity, with the solenoidal one remaining.

$$\tilde{u_i'} = \tilde{u_i'} - \frac{k_j \tilde{u_j'}}{k_l k_l} k_i. \tag{3.4}$$

Thus we have

$$\tilde{u_i'} k_i = (\tilde{u_i'} - \frac{k_j \tilde{u_j}}{k_l k_l} k_i) k_i = \tilde{u_i'} k_i - k_j \tilde{u_j'} = 0, \tag{3.5}$$

which is the sufficient condition for the field to satisfy continuity equation in spectral space.

Then the discretized energy spectrum of current turbulence field can be expressed as

$$E(k) = \sum_{k-\Delta k/2 \le \sqrt{k_1^2+k_2^2+k_3^2} < k+\Delta k/2} \frac{\tilde{u_j}(k_1,k_2,k_3)\tilde{u_j}(k_1,k_2,k_3)}{2} \tag{3.6}$$

where k=0,1,2,...,k_{max},

$$k_{max} = max\{\sqrt{k_1^2+k_2^2+k_3^2}\} \tag{3.7}$$

and increment

$$\Delta k = \frac{k_{max}}{N_E}, \tag{3.8}$$

with N_E being the total number of k.

Step 4 enforces $\tilde{u_i'}$ to conform with a specified energy spectrum E_{des},

$$\tilde{u_i'}(k_1,k_2,k_3) = \sqrt{\frac{E_{des}(k)}{E(k)}}\tilde{u_i'}(k_1,k_2,k_3), k-\Delta k/2 \le \sqrt{k_1^2+k_2^2+k_3^2} < k+\Delta k/2. \tag{3.9}$$

The resulting fluctuating velocities will fulfil the desired energy spectrum by itself since up to here

$$E = \frac{\tilde{u_j'}\tilde{u_j'}}{2} = \frac{\sqrt{\frac{E_{des}}{E}}\tilde{u_j'}\sqrt{\frac{E_{des}}{E}}\tilde{u_j'}}{2} = \frac{\frac{E_{des}}{E}\tilde{u_j'}\tilde{u_j'}}{2} = \frac{E_{des}}{E}E = E_{des}. \tag{3.10}$$

Step 5 performs an inverse fast Fourier transformation (IFFT) with $\tilde{u_i'}$ to get an elementary distribution of turbulence field that is both divergent-free and energy-spectrum-satisfied. (**ifftn**)

Step 6 multiplies u_i' by a factor (C) to increase or decrease the u_i''s root-mean-square (RMS) as wished. The RMS of u_i' is defined as

$$rms\{u_i'\} = \sqrt{< u_i'u_i' >}, \tag{3.11}$$

which reflects the turbulence intensity of the inlet velocity profile.

Step 7 extracts the 2D u_i' distribution on an n_3 plane as the fluctuating part of inflow velocities in Eq. 3.1.

Step 8 combines 2D fluctuating velocities u_i' and mean velocities U_i to get the target turbulent inlet u_i.

3.3 Application Studies

Turbulent inlet produced using the approach described in the previous section is applied to re-simulate the turbulent jets [5], to observe the performance of rectangular jets with high Reynolds numbers, through MRT-LBM-LES.

The eddy viscosity ν_t is calculated from the filtered strain rate $S_{ij} = (\partial_j u_i + \partial_i u_j)/2$ and a filter length scale δ_X, to implement the Smagorinsky model [41, 42], as follows:

$$\nu_t = (c_s \delta_X)^2 S, \tag{3.12}$$

$$S = \sqrt{\langle S_{ij} S_{ij} \rangle}. \tag{3.13}$$

Eddy viscosity ν_t and the effective kinematic viscosity ν^* of LES are introduced and related by

$$\nu^* = \nu + \nu_t, \tag{3.14}$$

where ν_t can be calculated by previously discussed Smagorinsky model [Eqs. 3.12 and 3.13]. Then we have the formulas to compute the effective viscosity and s_9^*:

$$\nu^* = \frac{1}{3}(\frac{1}{s_9^*} - \frac{1}{2}) c \delta_X \tag{3.15}$$

and

$$s_9^* = \frac{2 c \delta_X}{6\nu^* + c\delta_X}. \tag{3.16}$$

For the implementation of LES, bulk viscosity ζ is introduced:

$$\zeta = \frac{2}{9}(\frac{1}{s_1} - \frac{1}{2}) c \delta_X. \tag{3.17}$$

By using the strain rate from the previous time step to calculate ν_t in Eqs. 3.12 and 3.13, the scheme's simplicity and numerical accuracy are well-preserved at the same time [43].

As we are investigating turbulent rectangular jets, we will manipulate time-mean velocities and half-widths derived from them, U, V, W, U_{cl}, Y_h and Z_h, instead of instantaneous ones as examined in laminar jet study.

3.3.1 Axis-switching in A Turbulent Jet with $AR = 1.5$

We have closely looked at axis-switching phenomenon in Chapter 2 when studying low-Reynolds-number laminar rectangular jets. Yet we are also curious if axis-switching will be present in turbulent jets and how they will look like, especially when our just developed turbulent inlet is implemented. In general, the turbulent jets investigated in this and later chapters share the same set-up as in the laminar jet study in Chapter 2. Chapter 1 can be referred to for details such as geometric configurations and boundary conditions.

For the observation and comparison of axis-switching phenomenon with and without turbulence at the inlet, we perform MRT-LBM-LES of two $AR = 1.5$ turbulent rectangular jets with identical set-up except for the inflow condition. To be specific, the computation domain measures $90 \times 60 \times 450$ in lattice unit while jet exit is 12×8 in dimensions. Jet with a laminar inlet issues with a uniform velocity profile $U_0 = 39.0m/s$, while jet with turbulent inlet starts from the slot with a bonus u_i' with $I = 5\%$, in addition to a uniform MSV $U_i = U_0 = 39.0m/s$. The fluid's kinematic viscosity $\nu = 1.51e-5(m^2/s)$, so Reynolds number characterized by the height of jet ($h = 0.01m$) gets to 25900. Here I is a quantity that describes the inlet turbulence intensity, defined as

$$I = \frac{\sqrt{\langle u_i' u_i' \rangle}}{U_x(0,0,0)}, \tag{3.18}$$

where $U_x(0,0,0)$, here equal to U_0, denotes the laminar part of streamwise velocity at the center of the inlet. Continuity equation is enforced as well as a specified energy spectrum prescribed by

$$E_{des} = C\frac{k^6}{(1+\frac{k}{60})^{12}}, C = 0.00009, \tag{3.19}$$

where the adjusting factor C is already incorporated to yield the just indicated I.

Fig. 3.2 shows the HWCs at two specified downstream locations for each jet. By comparing the line marked with a later location, it is seen that, with the same Reynolds number, the ratio of longer to short axis in the case of turbulent inlet (b) is larger than that in the laminar inlet (a). So it is concluded that the current turbulent

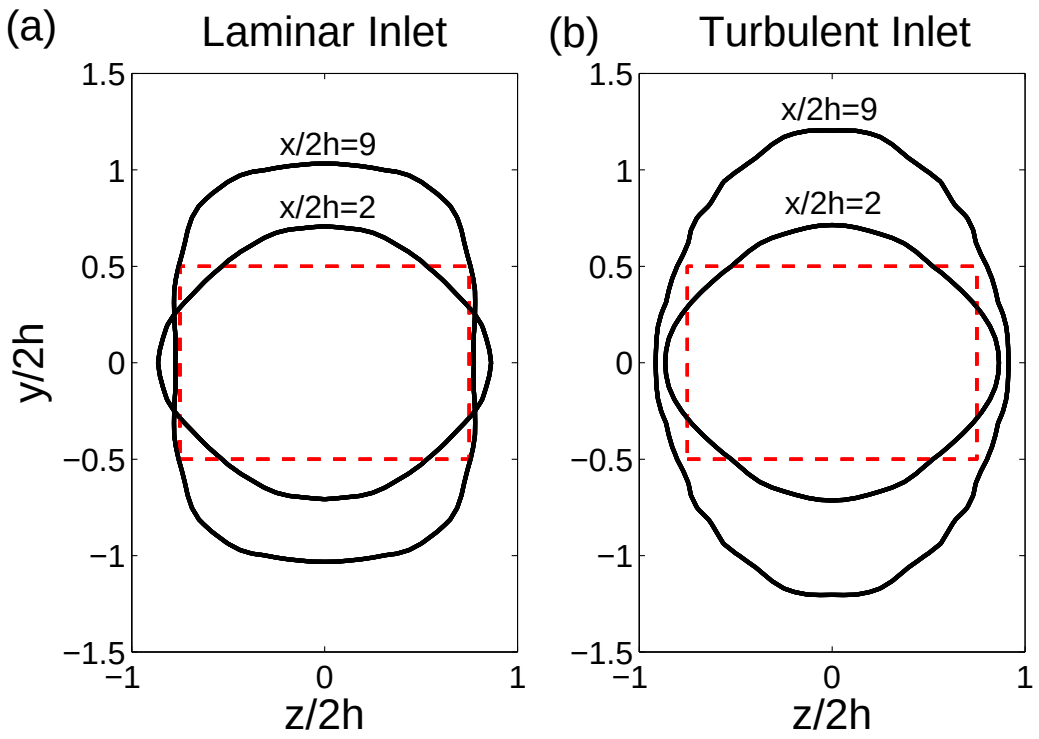

Figure 3.2. Comparison of axis-switching between rectangular jets with (a) laminar and (b) turbulent inlet profiles. The turbulent inlet profile generates axis-switching in much better agreement with experiment [4]. Red dashed line: jet inlet; black solid line: HWC at selected downstream locations ($x/2h = 2$ and $x/2h = 9$).

jet with the turbulent inlet presents more profound axis-switching phenomenon than the other one with a laminar inlet. In fact, Fig. 3.2 (b) agrees well with what was captured in the experiment [4]. As axis-switching reflects the intensity of flow mixing, it might be appropriate to say turbulence-involved inflow enhances flow mixing and entrainment during the jet development.

3.3.2 Square Jets

As mentioned at the beginning of this chapter, previous LBM study of a turbulent square jet didn't achieve quantitative agreement with Quinn's experimental data [39], for such aspects as centerline MSV decay and turbulence levels. Due to the fact that 0.5% of turbulence was supplied at the center of the slot exit plane in Quinn's experiment as compared to a laminar inflow in the computation investigation, it is suspected that the disagreement comes from the different inlet conditions applied to the separate study. Additionally, there exists an assumption that replacing the laminar inlet with a comparable turbulent one to that in Quinn's experiment, could possibly improve the degree of agreement between the two investigations. For the purpose of validating this supposition, we revisit the square jet study with our newly developed turbulent inflow equipped. The studies of turbulent inlet and saddle-back velocity profile deal with rectangular jets with relatively large Reynolds numbers. Considering its better stability of characteristics and higher accuracy than its SRT brother and trying to avoid expensive computation cost, we apply multiple-relaxation-time model for large-eddy-simulation (MRT-LES) to conduct the turbulent jet investigations.

To begin with, the subject square jet of 20×20 sits in an $80 \times 80 \times 450$ channel in lattice unit. Jet height $h = 0.04m$ and U_i follows the distribution illustrated in Fig. 3.3, with $U_x(0, 0, 0) = 60.0m/s$, to be consistent with Quinn's experimental set-up. The fluid kinematic viscosity $\nu = 1.30e - 5(m^2/s)$, combined with $U_x(0, 0, 0)$ and h, gives $Re = 184000$. u_i' is so added that I varies from 0 to 10% by adjusting C in the following desired energy spectrum.

$$E_{des}(k) = C\frac{k^\alpha}{k^{2\alpha} + k_0^{2\alpha}}, \alpha = 2, k_0 = 2. \tag{3.20}$$

We now compare our simulations results with Quinn's experimental results in four different aspects.

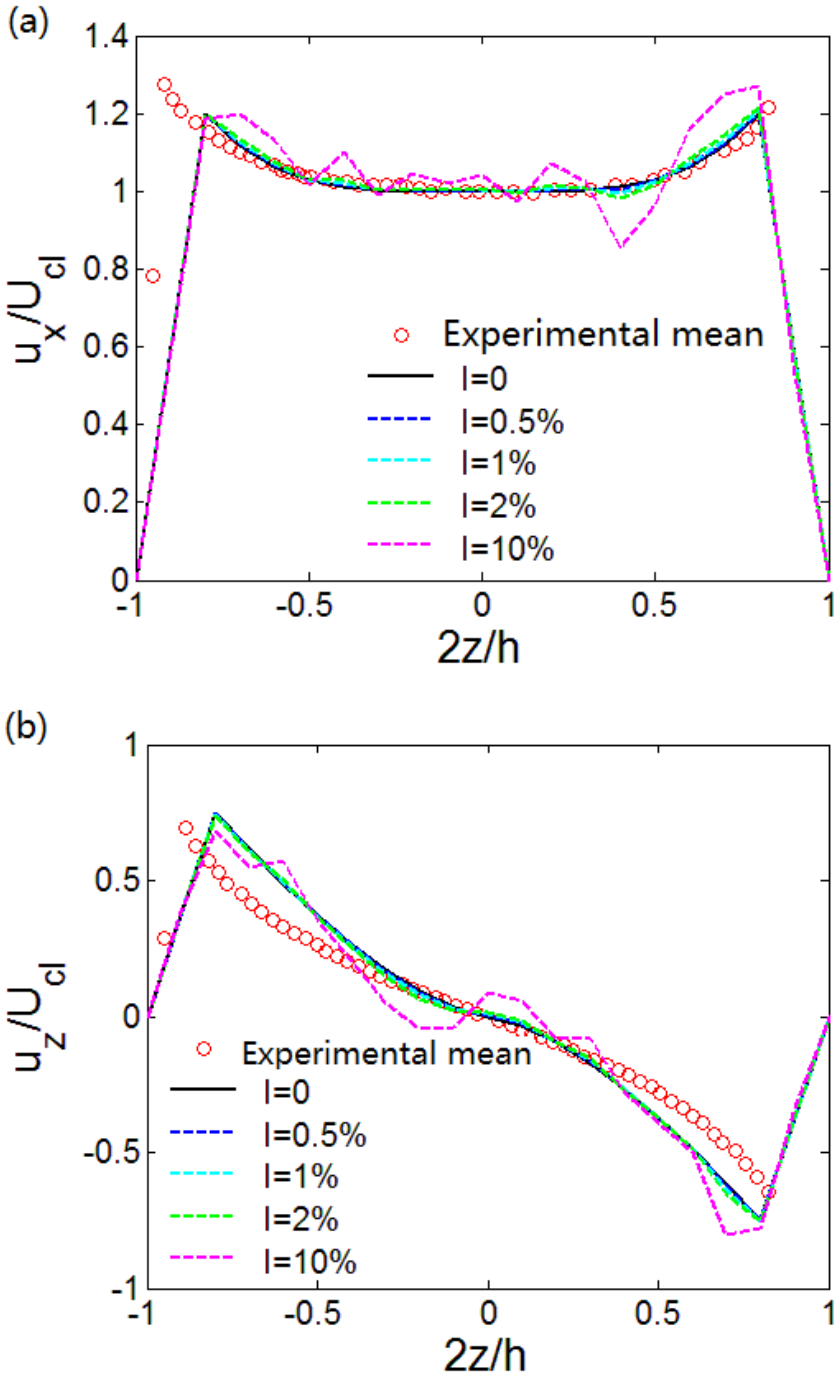

Figure 3.3. Inlet velocity profiles with different I: (a) streamwise, (b) spanwise. Circles: experimental mean velocities [39], black solid lines: $I = 0$; purple dashed lines: $I = 0.5\%$; blue dashed lines: $I = 1\%$; purple dashed lines: $I = 2\%$; purple dashed lines: $I = 10\%$.

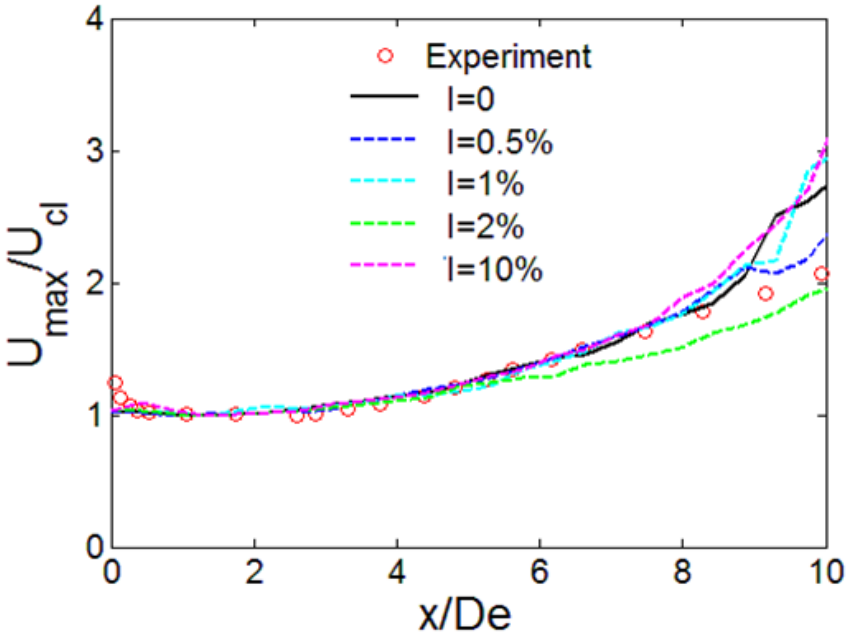

Figure 3.4. Inverse normalized mean centerline velocity decay of square jets with different I. Circles: experiment [39], black solid lines: $I = 0$; purple dashed lines: $I = 0.5\%$; blue dashed lines: $I = 1\%$; purple dashed lines: $I = 2\%$; purple dashed lines: $I = 10\%$.

A. Velocity Decay

Firstly, we check the velocity evolution along the centerline downstream for jets with different I levels. Curves for inverse normalized mean centerline velocity U_{max}/U_{cl} against normalized streamwise displacement x/De are shown in Fig. 3.4, where

$$U_{cl} = U_x(x, 0, 0), \tag{3.21}$$

and

$$U_{max} = max\{U_{cl}\}, \tag{3.22}$$

D_e stands for the equivalent diameter of the rectangular jet to a round one with the same area, calculated by

$$D_e = 2\sqrt{wh/\pi}. \tag{3.23}$$

As can be seen in the graph, jets with all levels of I at the inlet align quite well with Quinn's observations of the centerline velocity evolution. However, we still observe the difference between simulations and experimental data for the region that is most close to the inlet ($x/D_e < 1$) to certain extent. And we are not able to decrease the disagreement no matter how much turbulence is added to the inlet.

B. Velocity Profile

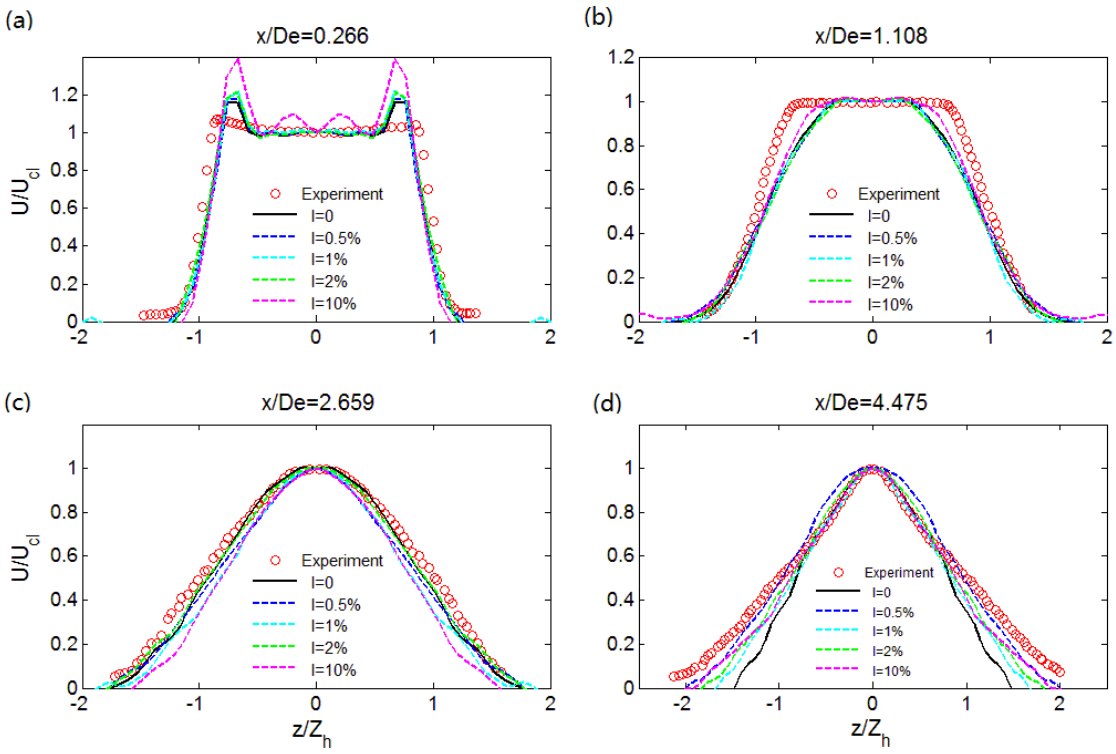

Figure 3.5. Normalized MSV distribution along spanwise axis at several downstream locations for square jets with different I. (a) $x/D_e = 0.266$, (b) $x/D_e = 1.108$, (c) $x/D_e = 2.659$, (b) $x/D_e = 4.475$. Circles: experiment [39], black solid lines: $I = 0$; purple dashed lines: $I = 0.5\%$; blue dashed lines: $I = 1\%$; purple dashed lines: $I = 2\%$; purple dashed lines: $I = 10\%$.

Fig. 3.5 presents MSV profiles along spanwise axis at 4 selected downstream locations for the experiment and all simulation results. Once again, jet simulations of all I levels have rather close performance to Quinn's experiment. The shape of MSV distribution evolves gradually from flat-topped, resembling that issued from the exit, to parabolic when the flow has experienced thorough mixing with surrounding medium. However, no evident diversity is seen between with or without added turbulence, or how much turbulence is added. Therefore we conclude that MSV profiles are insensitive to the inflow types and our LBM simulations with all cases of I perform well as for the prediction of MSV profiles.

C. Half-width Growth

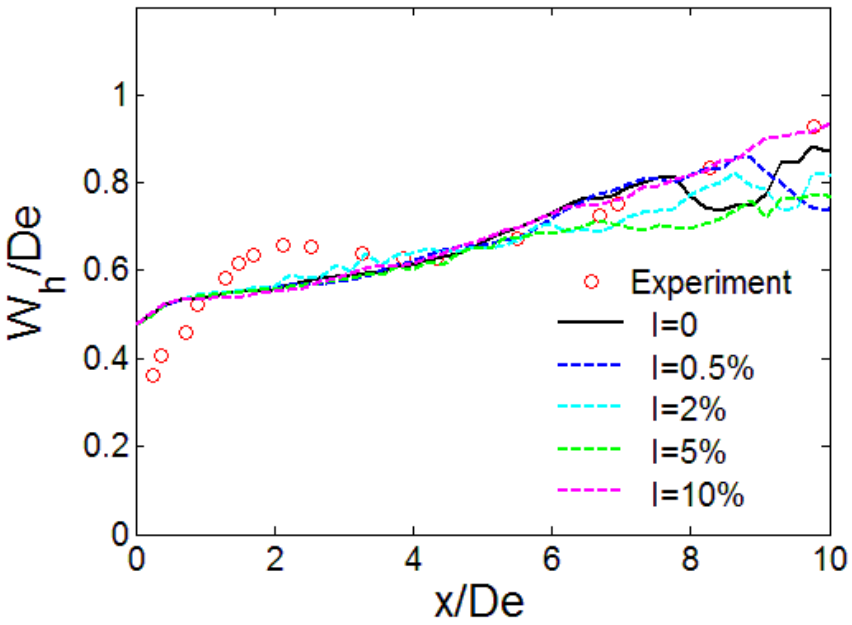

Figure 3.6. Half-width growth downstream for square jets with different I. Circles: experiment [39], black solid lines: $I = 0$; purple dashed lines: $I = 0.5\%$; blue dashed lines: $I = 1\%$; purple dashed lines: $I = 2\%$; purple dashed lines: $I = 10\%$.

Jet's half-width (W_h) is determined by

$$W_h =< \sqrt{y_{\frac{1}{2}}^2 + z_{\frac{1}{2}}^2} >, \tag{3.24}$$

where $\langle \cdots \rangle$ takes the average over space of its argument, $y_{\frac{1}{2}}$ and $z_{\frac{1}{2}}$ satisfy

$$U(x, y_{\frac{1}{2}}, z_{\frac{1}{2}}) = \frac{1}{2} U_{cl}. \tag{3.25}$$

Comparison of half-width growth downstream illustrated in Fig. 3.6 says that, for the near-inlet field ($x/D_e < 4$), simulation curves' deviation from experiment data of either direction is obvious. So it means the appliance of turbulent inlet still fails to capture jet expansion features in the most near field. However jet simulation with $I = 10\%$ does a good job in predicting the monotonic growth of jet in contrast of experiment data. It might be safe to say the addition of turbulence to the inflow could improve the agreement with experiment for the far range of near field.

D. Turbulent Intensity Profile

Streamwise turbulence profile is another aspect that was mentioned to be unsatisfactory in the previous work. So we highly look forward to addressing this issue by trying various levels of turbulence to the inflow. However, we are not able to decrease the magnitude evidently however much I is applied. Although the shapes of profiles are similar to the experimental counterparts (Fig. 3.7), there exists noticeable gaps between curves from simulations and experiment, especially for closer planes to the jet exit. We attribute this deficit to the fact that the inflow condition can still not be guaranteed to be identical to experimental set-up. In the experiment only the turbulence intensity in the center is given, while how it is distributed all over the plane remains a mystery. In the near future, we might try turning to a temporal turbulence distribution rather than the spatial one currently used, to see if any improvement will be observed.

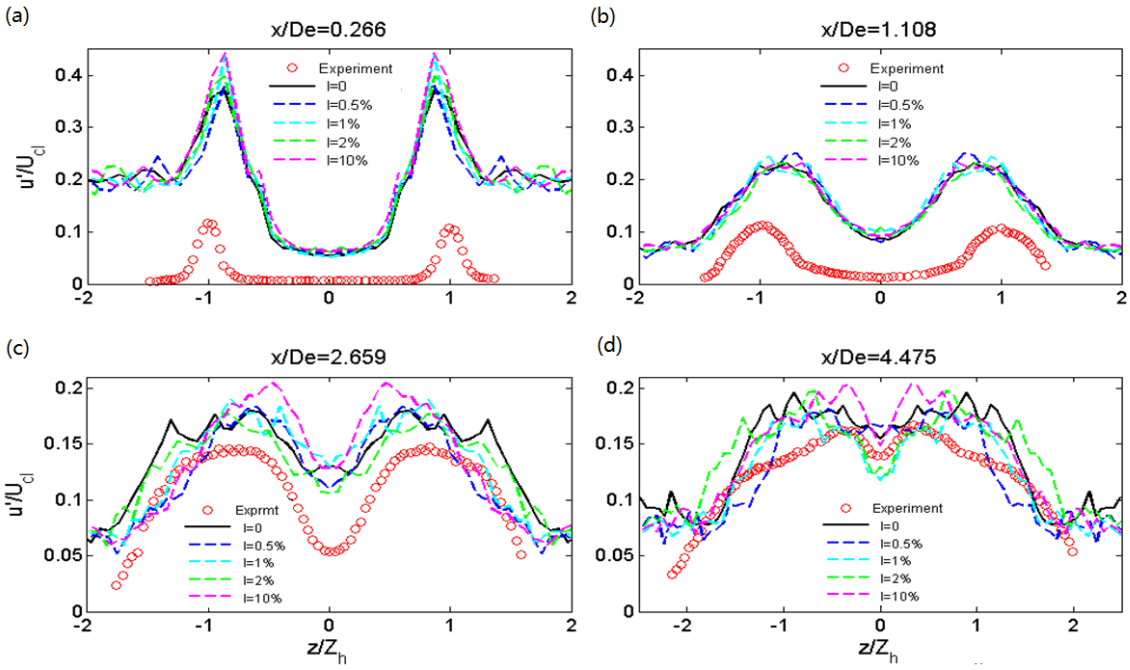

Figure 3.7. Normalized streamwise turbulence intensity profiles along spanwise axis at several downstream locations for square jets with different I. (a) $x/D_e = 0.266$, (b) $x/D_e = 1.108$, (c) $x/D_e = 2.659$, (b) $x/D_e = 4.475$. Circles: experiment [39], black solid lines: $I = 0$; purple dashed lines: $I = 0.5\%$; blue dashed lines: $I = 1\%$; purple dashed lines: $I = 2\%$; purple dashed lines: $I = 10\%$.

Summary

In order to validate the conclusion made by past work [5] and improve our ability to predict turbulent jets, we develop turbulent inlet velocity profiles inspired by Petersen's Ph.D. dissertation [40]. Characteristic comparisons of five jets driven by laminar and turbulent inlets are performed. Although the turbulent inlets well captured the near field velocity decay and velocity profiles, we did not see the improvement in terms of quantitative agreement of turbulence intensity profile with the experiment. Also, we were not able to match the centerline velocity evolution and half-width growth in the immediate proximity of jet exit with the actual experiment.

It is speculated that inconsistency still exists because the space-based turbulence in the inlet is not close enough to the actual turbulence added in the experiment. We look forward to the development of more realistic turbulent inlet profiles and come back to this subject again in the future.

4. CHARACTERISTICS OF SADDLE-BACK VELOCITY PROFILE IN TURBULENT RECTANGULAR JETS

4.1 Description

Saddle-back velocity profile in rectangular jets, which is regarded as another peculiar behavior, has been reported in quite a few experiments and computations [4, 6–8, 19, 37, 38, 44–46]. Saddle-back velocity profile is typically a behavior in rectangular with relatively large AR, however, the mechanism triggering such a behavior during the jet revolution is not clear.

In the case of $AR = 5$, Tsuchiya [4] reported saddle-back velocity profile along spanwise axis in his experiment, whereas another experiment by Quinn [46] did not capture evident such a profile. Previously Yu et al. [5] also numerically studied a same $AR = 5$ jet, but did not capture such a profile profoundly by using a laminar inlet velocity profile. We now use the developed turbulent inlet velocity profile to study a group of turbulent rectangular jets with varying AR to explore the mechanism of this behavior. Their configurations are listed Table 4.1. The turbulent inlet velocity field satisfies energy spectrum defined in Eq. 3.20.

Table 4.1. Jet configurations with varying AR. The unit for length is meter(m).

Jet	AR	I	b, h	B, H, L	jet grid size	Domain grid size
A	2	3%	$0.01, 0.02$	$0.108, 0.043, 0.325$	$28, 14$	$150, 60, 450$
B	3	3%	$0.01, 0.03$	$0.108, 0.043, 0.325$	$42, 14$	$150, 60, 450$
C	4	3%	$0.01, 0.04$	$0.108, 0.043, 0.325$	$56, 14$	$150, 60, 450$
D	5	3%	$0.01, 0.05$	$0.108, 0.043, 0.325$	$70, 14$	$150, 60, 450$
E	6	3%	$0.01, 0.06$	$0.108, 0.043, 0.325$	$84, 14$	$150, 60, 450$

4.2 Results

We begin with the study of one turbulent jet with $AR = 5$ through MRT-LBM-LES using the developed turbulent inlet profile. After the saddle-back velocity profile is identified, the underlying mechanism is obtained by comparison of normalized streamwise velocity and turbulence intensity fields. Then we define two parameters, profound saddle-back range and peak-center difference, to quantify the magnitude of saddle-back, which enables us to compare the saddle-back velocity profile of rectangular jets with different AR and turbulence intensity at the turbulent inlet I.

4.2.1 Mechanism of Saddle-back Velocity Profile

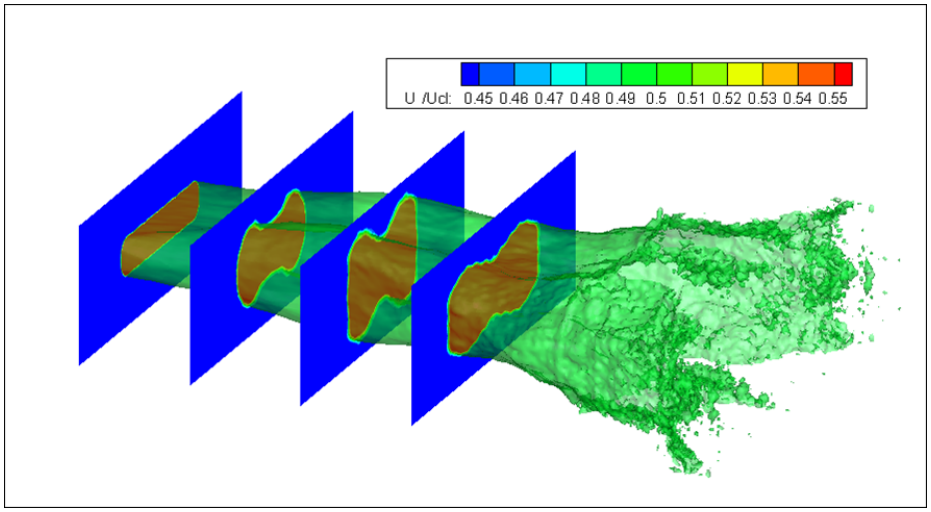

Figure 4.1. Normalized MSV iso-surface ($U/U_{cl} = 0.5$) and selected cross-sectional normalized MSV field for $AR = 5$, $I = 3\%$.

Fig. 4.1 describes the development of the jet entrainment through an iso-surface of normalized MSV in general. Contours on the cross-sectional planes at different downstream locations present the jet propagation. To avoid the complex boundary effects, we only look at the characteristics within the near-field. The near-field is

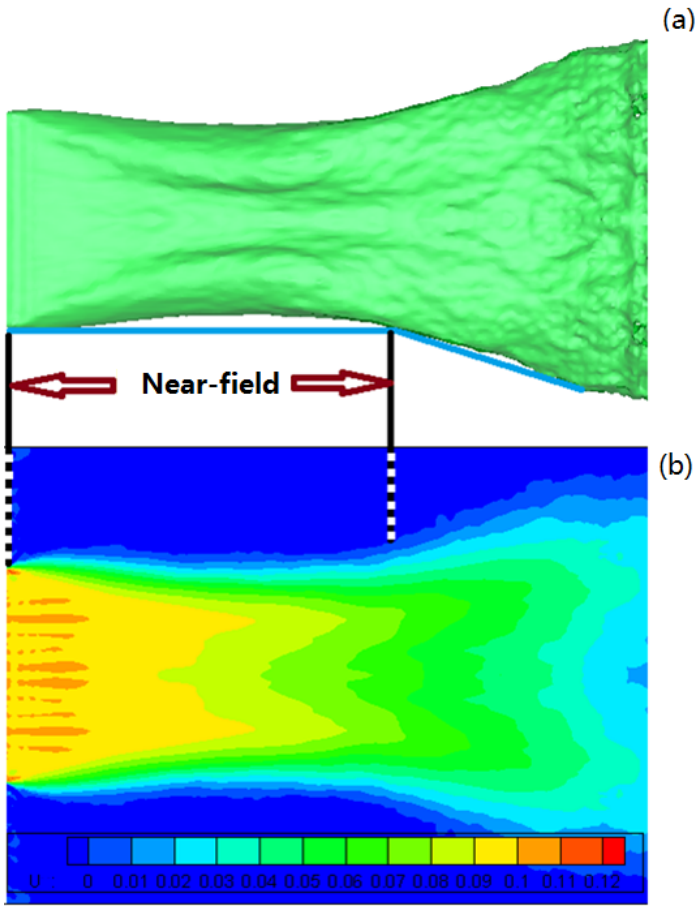

Figure 4.2. Near-field illustration on (a) iso-surface ($U/U_{cl} = 0.5$) and (b) MSV field of spanwise axis plane, for $AR = 5$, $I = 3\%$.

defined from the inlet until the spanwise ends of the jet start to diverge as illustrated in Fig. 4.2.

In Fig. 4.3, four positions downstream are selected to check the normalized MSV profiles along spanwise axis. The jet shape evolves from initially a flat top to a clear central recessed saddle-back as seen in Fig. 4.3. Tsuchiya [4] compared the velocity and turbulence intensity distribution and noticed that the peaks of mean velocity correspond to the local minimum turbulence intensity as shown in Fig. 4.4. It was thought that the saddle-back velocity profile is resulted from a mixing-retarded region as compared its surroundings. Inspired by this hint, we compare the normalized

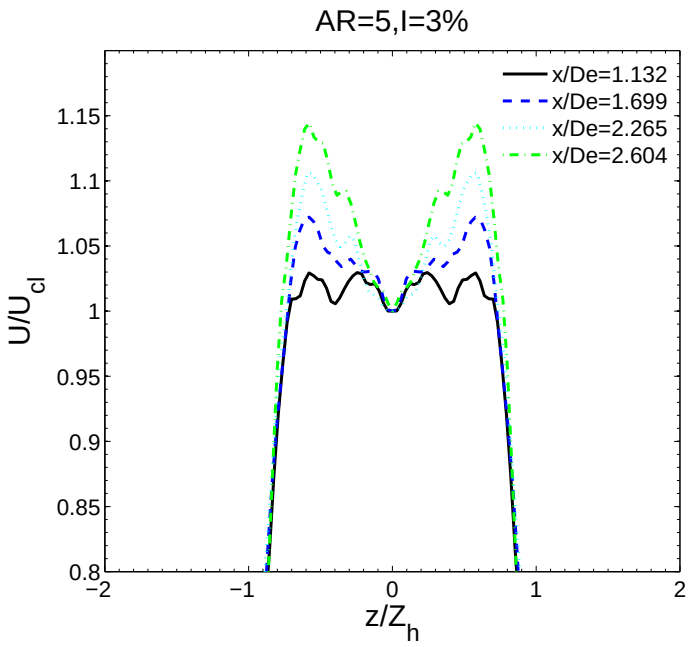

Figure 4.3. Evolution of normalized MSV profile at representative downstream locations for $AR = 5$, $I = 3\%$. Black solid line: $x/D_e = 1.132$, blue dashed line: $x/D_e = 1.699$; cyan dotted line: $x/D_e = 2.265$; green dash-dot line: $x/D_e = 2.604$.

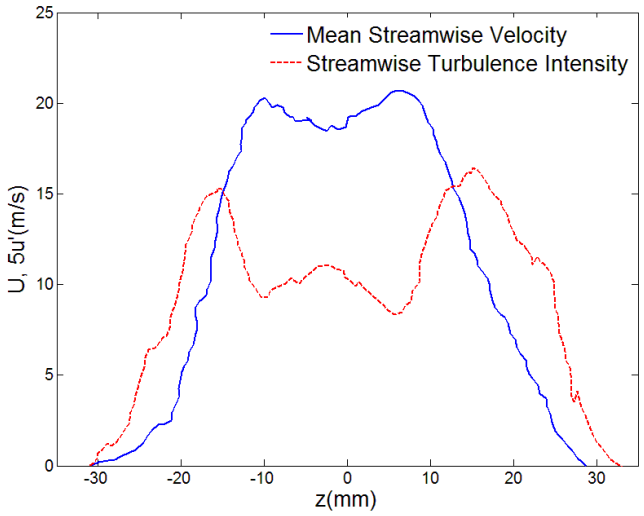

Figure 4.4. Saddle-back profile explanation by Tsuchiya [4]. Blue solid line: MSV profile; red dashed line: streamwise turbulence profile.

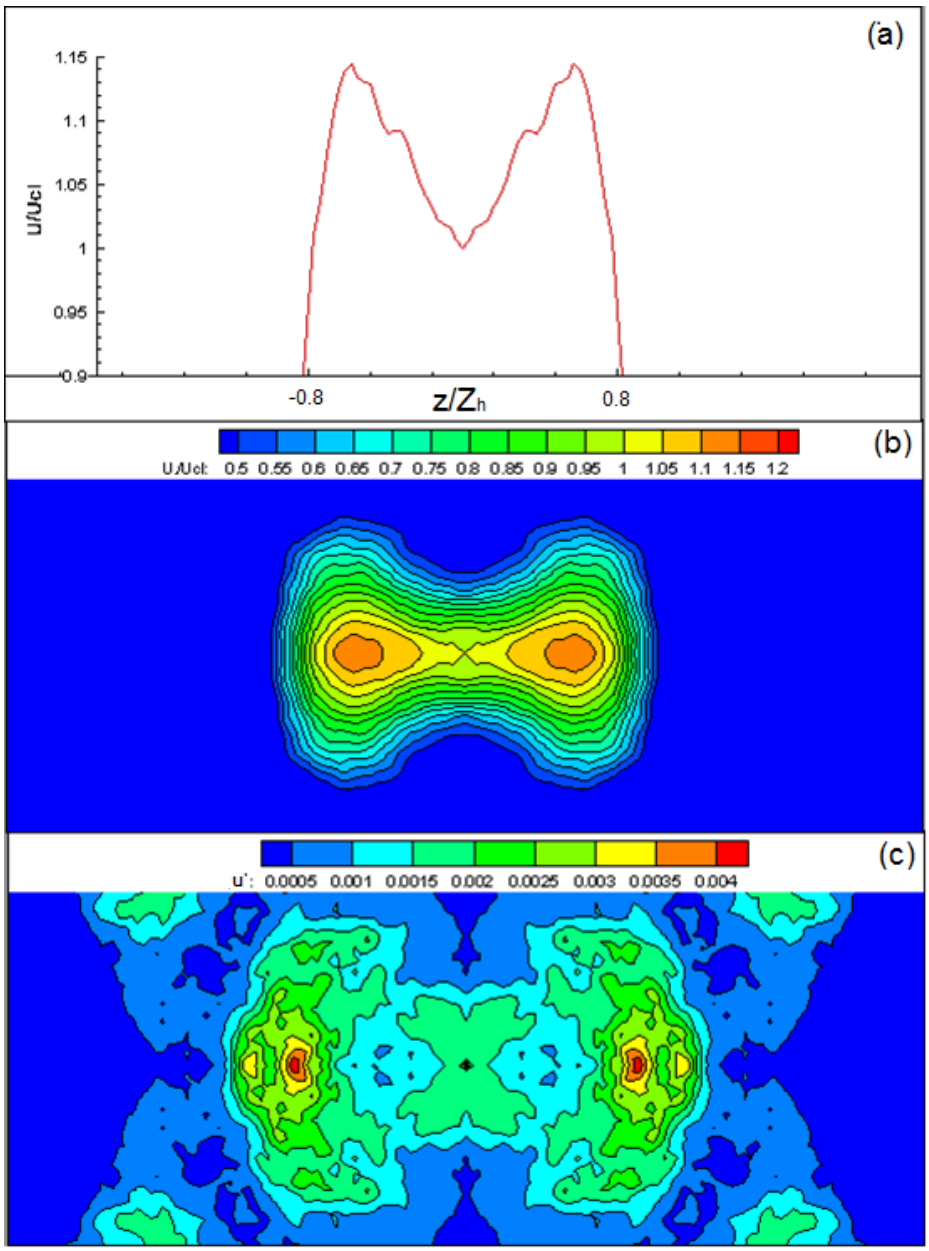

Figure 4.5. (a) Saddle-back velocity profile, (b) normalized MSV field and (c) streamwise turbulence intensity field at the same downstream laocation $x/D_e = 2.60$, for $AR = 5$, $I = 3\%$. The figures share the same horizontal axis as showed in (a).

MSV and streamwise turbulence intensity field, where saddle-back velocity profile presents at the same downstream location (Fig. 4.5). It is then confirmed that the

peak velocities correspond to the minimum turbulence intensity in the surrounding regions. If it is true that streamwise turbulence intensity reflects local mixing level, the saddle-back velocity profile becomes understandable as the two regions acquire largest mean streamwise velocities thanks to the weakest mixing activity among their neighborhoods. Therefore, our simulation results agree with Tsuchiya's statement of saddle-back velocity profile.

4.2.2 AR Effect on Saddle-back Velocity Profile

We now quantify saddle-back velocity profile by defining two parameters, the first of which is called peak-center (Δ_{pc}) difference defined as

$$\Delta_{pc} = max\{\frac{U_{peak} - U_{cl}}{U_{cl}} \times 100\%\}, \tag{4.1}$$

where U_{peak} and U_{cl} denote the velocity at the peaks and center of the saddle-back profile respectively; $max\{\cdots\}$ means the largest difference among the profiles at all near-field downstream locations is taken as the Δ_{pc}. If $\Delta_{pc} \geq 10\%$, we call the velocity profile as a profound sadd-back (PSB). Then the second quantifying parameter PSB range is defined as the normalized streamwise length where PSB is observed. Fig. 4.6 shows how to determine the PSB range on the normalized MSV field of the spanwise axis plane. Next, we compare the intensity of saddle-back velocity profile for jets with different configurations. First, in an attempt to find out AR's effect on the degree of saddle-back velocity profile, we conduct simulations for six rectangular jets, with AR ranging from 2 to 7 with the same turbulence intensity at the inlet, domain dimension and grid size in Table 4.1.

It is seen that saddle-back velocity profile occurs in all jets in Fig. 4.7. This observation is a supplementation to previous statement that saddle-back velocity profile was only seen in large-AR jets, as saddle-back velocity profile even occurs for the $AR = 2$ jet in our study. Moreover, with the increase of AR, the intensity of saddle-back-profile becomes more significant. Δ_{pc} for each case is calculated by Eq. 4.1 after U_{peak} and U_{cl} are obtained from the profiles in Fig. 4.7. We obtain the PSB

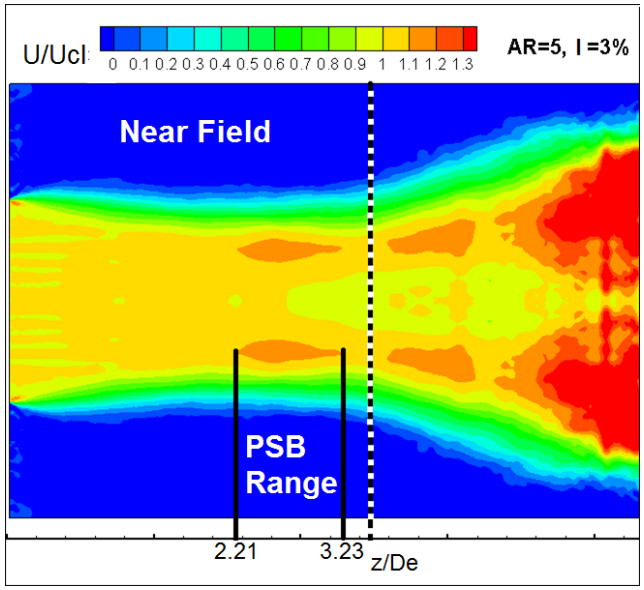

Figure 4.6. Measurement of PSB range on the normalized MSV field of the spanwise axis plane.

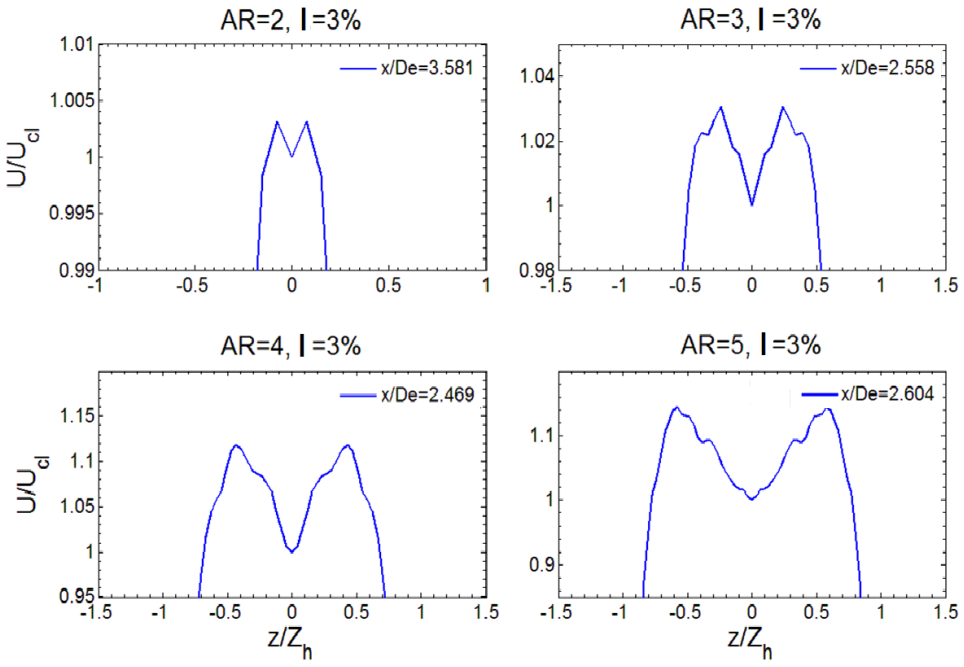

Figure 4.7. Most profound saddle-back velocity profiles and corresponding downstream locations for jets with different AR.

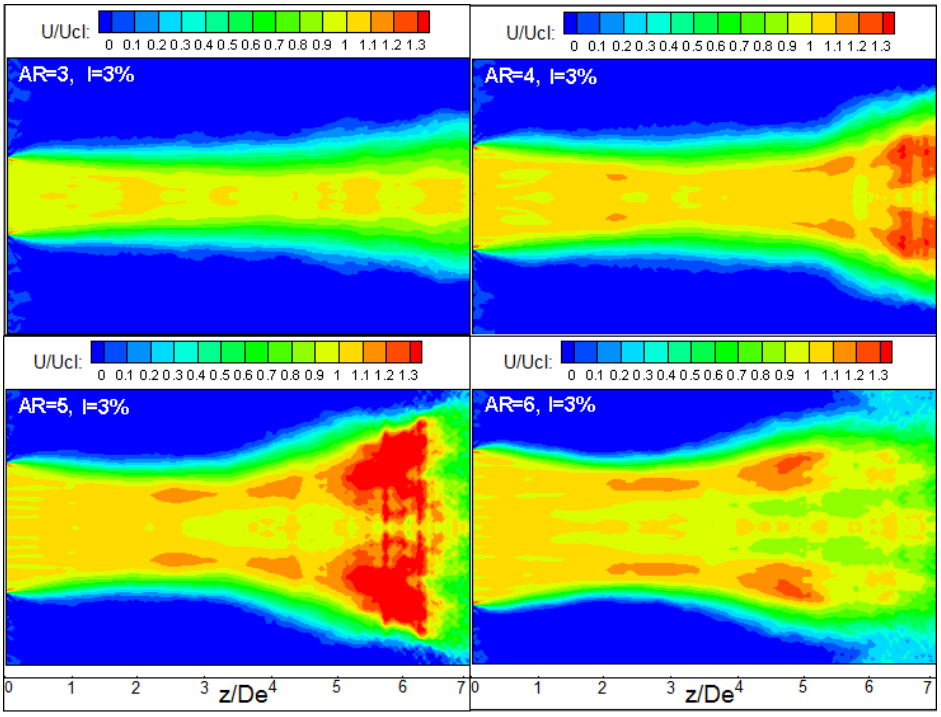

Figure 4.8. Normalized MSV field of the spanwise axis plane for different AR.

range by , identifying the start and end location for PSB on the normalized MSV field of the spanwise axis plane for each jet in Fig. 4.8. These two essential parameters are recorded and graphed in Fig. 4.9 for varying AR.

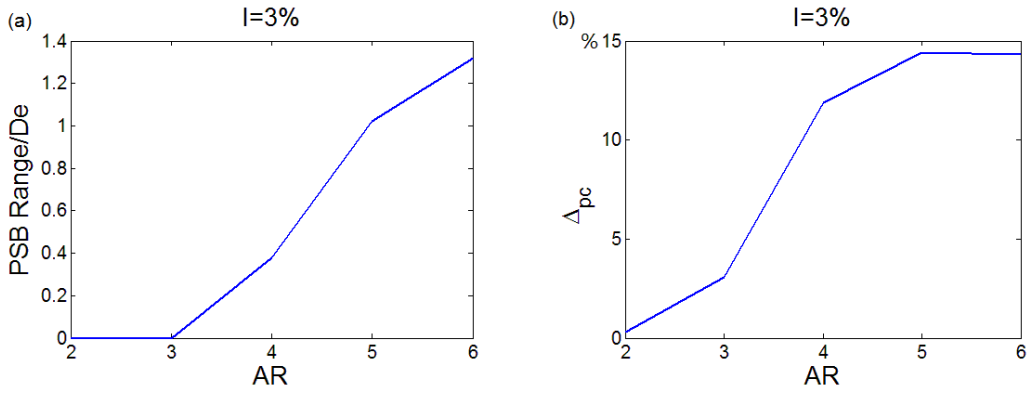

Figure 4.9. AR effect on: (a) PSB range, (b) peak-center difference.

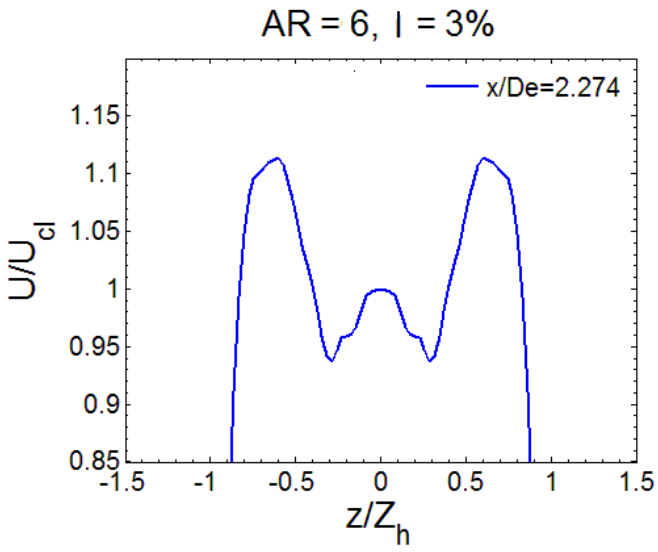

Figure 4.10. Dual saddle-back velocity profile for $AR = 6$, $I = 3\%$.

It is seen that both Δ_{pc} and PSB range increase with larger AR. As saddle-back velocity profile reflects an uneven distribution of mixing levels, this trend might imply a higher mixing intensity for slimmer rectangular jets. Yet we notice Δ_{pc} of $AR = 6$ jet slightly shrinks compared to $AR = 5$, which somehow deviates from the overall trend. After a closer look at the MSV profile with the strongest saddle-back for $AR = 6$ jet (Fig. 4.10), we notice that our Δ_{pc} formula is not suitable for measuring its particular dual saddle-back shape, as the profile has two distinctive lowest points around the centre compared to only one for the other cases. Thus, an alternative formula for Δ_{pc} is required to quantify this special kind of saddle-back profile more accurately, which we might continue to search for in the future.

4.2.3 Effect of Turbulence Intensity at the Inlet on Saddle-back Velocity Profile

Now we also study the effect of turbulence intensity at the Inlet for six jets with $AR = 5$. The variation of I is listed in Table 4.2. PSB range and peak-center difference are examined and compared. All I levels present saddle-back velocity

Table 4.2. Jet configurations with varying I. The unit for length is meter(m).

Jet	AR	I	b, h	B, H, L	jet grid size	Domain grid size
a	5	0	$0.01, 0.05$	$0.108, 0.043, 0.325$	$70, 14$	$150, 60, 450$
b	5	0.5%	$0.01, 0.05$	$0.108, 0.043, 0.325$	$70, 14$	$150, 60, 450$
c	5	2%	$0.01, 0.05$	$0.108, 0.043, 0.325$	$70, 14$	$150, 60, 450$
d	5	3%	$0.01, 0.05$	$0.108, 0.043, 0.325$	$70, 14$	$150, 60, 450$
e	5	4%	$0.01, 0.05$	$0.108, 0.043, 0.325$	$70, 14$	$150, 60, 450$
f	5	5%	$0.01, 0.05$	$0.108, 0.043, 0.325$	$70, 14$	$150, 60, 450$

profile of different degrees (Fig. 4.11). PSB range measurement within the near field is feasible by checking the normalized MSV contours in Fig. 4.12, although some cases present a more complicated pattern of contour.

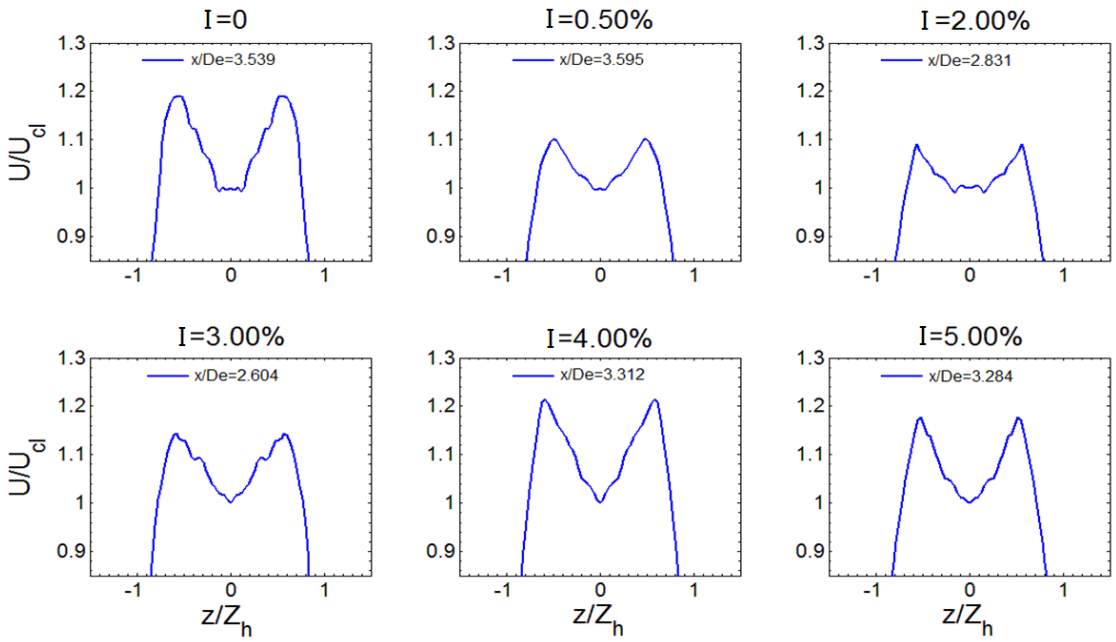

Figure 4.11. Most profound saddle-back velocity profiles and corresponding downstream locations for jets with different I.

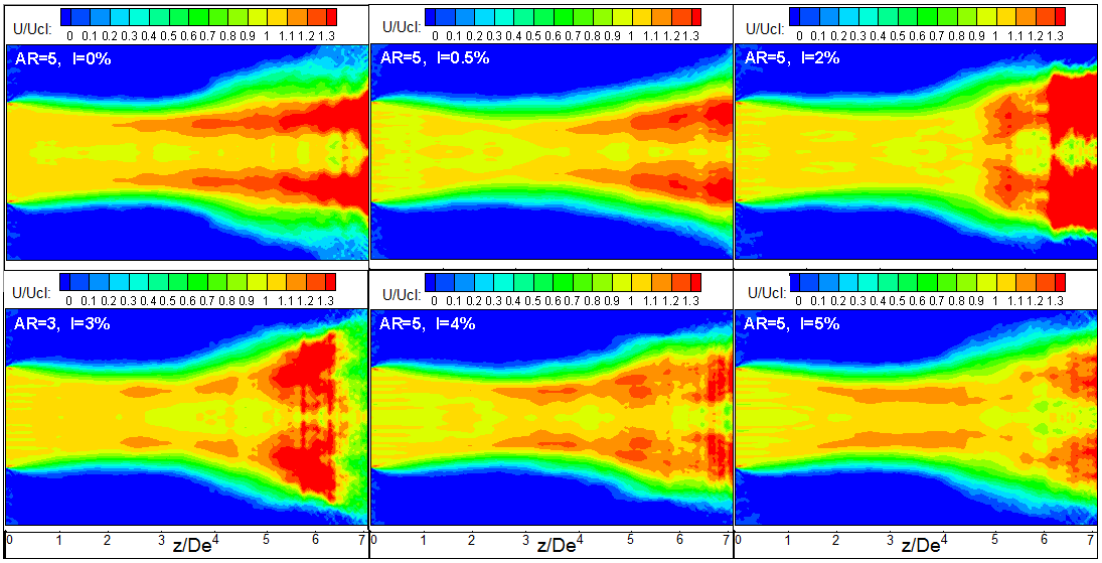

Figure 4.12. Normalized MSV field of the spanwise axis plane for different I.

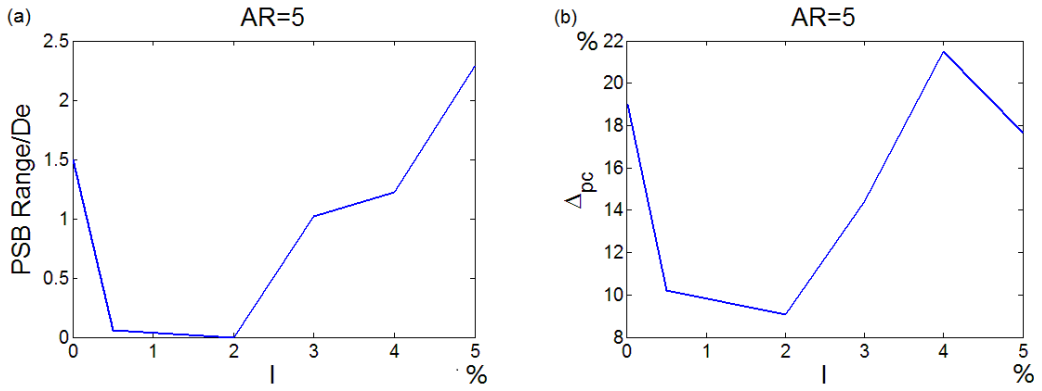

Figure 4.13. I effect on: (a) PSB range, (b) peak-center difference.

Different from AR effect, neither Δ_{pc} or PSB range presents a monotonic variation as I increases. However, a minimum Δ_{pc} and PSB range are obtained when $I = 2\%$. It seems that $I = 2\%$ leads to the weakest flow mixing intensity among all supplied I levels. But the underlying mechanism for the least profound saddle-back velocity profile and mixing showing up for an intermediate level of I is yet to be revealed.

4.3 Conclusions and Discussion

This chapter starts with a $AR = 5$ jet investigation, we are able to capture the saddle-back velocity profile for jets of AR ranging from 2 to 6. Tsuchiya's explanation for saddle-back phenomenon is confirmed by our own examination. It has been noted that the saddle-back's peak velocities are due to the local minimum mixing intensity. In order to quantify the saddle-back, we define two parameters to compare saddle-back velocity profile between different AR and turbulence intensity at the inlet. It is found that saddle-back is more profound with larger AR or slimmer rectangular jets, while its relation with I is still vague.

5. SUMMARY AND FUTURE WORK

In this thesis, we numerically investigated the underlying physics of two peculiar phenomena, which are axis-switching and saddle-back velocity profile, in both laminar and turbulent rectangular jets using lattice Boltzmann method (LBM). Previously developed computation protocols based on single-relaxation-time (SRT) and multiple-relaxation-time (MRT) lattice Boltzmann equations are utilized to perform direct numerical simulation (DNS) and large eddy simulation (LES) respectively. The main work is summarized as follows.

In Chapter 2, the mechanisms of 45° and 90° axis-switching in laminar jets suggested the independence of axis-switching behavior to the Re number, whereas the downstream location where axis-switching occurs will vary for different Re numbers. Based on the current work plus a turbulent inlet velocity profile we have developed very recently, we plan to revisit the axis-switching in turbulent rectangular jets focusing on the Re number effects on axis-switching development in the next step.

In Chapter 3, step-by-step introduction to the generation of turbulent inflow condition is demonstrated. The resulting turbulence field is divergence-free, fulfils specified energy spectrum and is flexible to achieve desired turbulence intensity. The first application study shows Turbulent inlet leads to more profound axis-switching under the current conditions for the inflow and jet configuration, which might imply stronger mixing activity during jet development. The second application tries to improve the simulation's agreement with the experimental data of square jets. Both inflow types result in a good prediction of jet development as for centreline velocity decay, MSV profiles and half-width growth. However, the application of turbulent inlet profile fails to perform a better prediction as for the nearest field nearest characteristics.

In Chapter 4, saddle-back velocity profile is observed for all AR rectangular jets. The underlying mechanism is explained. In addition, quantitative measurement and

comparison between jets with different AR and I are performed. It is then found that magnitude of saddle-back becomes larger with the increase of AR in general, all though $AR = 6$ jet presents a more sophisticated profile. But, influence of turbulence intensity at the inlet on saddle-back is still uncertain.

This thesis proves that lattice Boltzmann method is a reliable alternative CFD approach to capture the characteristics of rectangular jets. Axis-switching phenomenon and saddle-back velocity profile are observed and the underlying mechanism for each behavior is discovered. AR effect on the two rectangular jet features is also examined. For better prediction for rectangular jet development, the turbulent inlet velocity profile is developed, which enhances axis-switching for a rectangular jet we studied. The effect of turbulence intensity at the inlet on the saddle-back profile is investigated. The understanding of rectangular jet characteristics and mixing features are much improved through our systematic study.

Beyond this thesis, we want to further explore jet physics and its applications in the following aspects:

- Axis-switching in turbulent rectangular jets and jets with more complicated shapes.
- Dual saddle-back velocity profile as observed in jet with $AR = 6$.
- Effects of energy spectrum and turbulence intensity at the inlet (I) on jet characteristic features, such as turbulence intensity profile, axis-switching and saddle-back velocity profile.
- Produce a more realistic time-dependent turbulent inlet velocity profile.
- Relate our discoveries on turbulent jet to the mixing process between fuel and air in the combustion engine.

LIST OF REFERENCES

LIST OF REFERENCES

[1] E. J. Gutmark, F. F. Grinstein, "Flow control with noncircular jets," *Annu. Rev. Fluid Mech.* 31 (1999) 239.

[2] E. Gutmark, K. C. Schadow, "Flow characteristics of orifice and tapered jets," *Phys. Fluids* 30 (1987) 3448–54.

[3] H. Yu, S. S. Girimaji, "Lattice Boltzmann equation simulation of rectangular jet ($AR = 1.5$) instability and axis-switching," *Physica A* 362 (2006) 151–157.

[4] Y. Tsuchiya, C. Horikoshi, T. Sato, "On the spread of rectangular jets," *Exp. Fluids* 4 (1986) 197.

[5] H. Yu, S. S. Girimaji, "Turbulent simulations of rectangular jets using lattice Boltzmann method," *Phys. Fluids* 17 (2005) 125106.

[6] G. F. Marsters, J. Fotheringham, "The influence of aspect ratio on incompressible turbulent flows from rectangular slots," *Aeronaut. Q.* 31 (1980) 285.

[7] G. F. Marsters, "Spanwise velocity distributions in jets from rectangular slots," *AIAA J.* 19 (1981) 148.

[8] W. R. Quinn, "Development of a large-aspect-ratio rectangular turbulent free jet," *AIAA J.* 32 (1994) 547.

[9] S. Chen, G. D. Doolen, "Lattice Boltzmann method for fluid flows," *Ann. Rev. Fluid Mech.* 30 (1998) 329.

[10] X. He, L.-S. Luo, "Lattice Boltzmann model for the incompressible Navier-Stokes equation," *J. Comput. Phys.* 88 (1997) 927.

[11] U. Frisch, B Hasslacher, Y. Pomeau, "Lattice-gas automata for the Navier-Stokes equation," *Phys. Rev. Lett.* 56 (1986) 1505–1508.

[12] Y. H. Qian, D. d'Humires, P. Lallemand, "Lattice BGK models for Navier-Stokes equation," *Europhys. Lett.* 17 (1992) 479.

[13] P. Lallemand, L.-S. Luo, "Theory of the lattice Boltzmann method: Dispersion, dissipation, isotropy, Galilean invariance, and stability," *Phys. Rev. E* 61 (2000) 6546.

[14] I Ginzburg, D d'Humieres, "Multireflection boundary conditions for lattice Boltzmann models," *Phys. Rev. E* 68 (2003) 066614.

[15] D. dHumires, I. Ginzburg, M. Krafczyk, P. Lallemand, L.-S. Luo, "Multiple-relaxation-time lattice Boltzmann models in three dimensions," *Proc. R. Soc. London, Ser. A* 360 (2002) 437.

[16] L.-S. Luo, "Theory of the lattice Boltzmann method: lattice Boltzmann models for nonideal gases," *Phys. Rev. E* 62 (2000) 4982–4996.

[17] P. M. Sforza, M. H. Steiger, N. Trentacoste, "Studies on three-dimensional viscous jets," *AIAA J.* 4 (1966) 800.

[18] P. M. Sforza, "A quasi-axisymmetric approximation for turbulent three-dimensional jets and wakes," *AIAA J.* 7 (1969) 1380.

[19] N. Trentacoste, P. M. Sforza, "Further experimental results for three-dimensional free jets," *AIAA J.* 5 (1967) 885.

[20] H. S. Husain, A. K. M. F. Hussain, "Controlled excitation of elliptic jets," *Phys. Fluids* 26 (1983) 2763.

[21] C. M. Ho, E. Gutmark, "Vortex induction and mass entrainment in a small-aspect-ratio elliptic jet," *J. Fluid Mech.* 179 (1987) 383.

[22] K. Toyoda, F. Hussain, "Vortical structures of noncircular jets," in: *Proceedings of the Fourth Asian Congress of Fluid Mechanics*, Hong Kong, 21–25 August 1989, pp. A117–A127.

[23] F. Hussain, H. S. Husain, "Elliptic jets. Part 1. Characteristics of unexcited and excited jets," *J. Fluid Mech.* 208 (1989) 257.

[24] S. B. Verma, E. Rathakrishnan, "Influence of aspect-ratio on the mixing and acoustic characteristics of plain and modified elliptic slot jets," *Aero. Sci. Tech.* 7 (2003) 451–464.

[25] J.-H. Yoon, S.-J. Lee, "Investigation of the structure of an elliptic jet using stereoscopic particle image velocimetry," *Meas. Sci. Technol.* 14 (2003) 2034–2046.

[26] W. Zhao, K. Kumar, A. S. Mujumdar, "Flow and heat transfer characteristics of confined noncircular turbulent impinging jets," *Drying Tech.* 22 (9) (2004) 2027–2049.

[27] V. D. Kasyap, D. Sivakumar, B. N. Raghunandan, "Flow and breakup characteristics of elliptical liquid jets," *Int. J. Multiphase Flow* 35 (2009) 8–19.

[28] D. H. Kwon, S. J. Lee, "Axis-switching of non-axisymmetric microdroplet ejected from inkjet with an elliptical nozzle," *Phys. Fluids* 23 (2011) 051703.

[29] G. Amini, A. Dolatabadi, "Axis-switching and breakup of low-speed elliptic liquid jets," *Int. J. Multiphase Flow* 42 (2012) 96–103.

[30] T. H. New, D. Tsovolos, "Vortex behaviour and velocity characteristics of jets issuing from hybrid inclined elliptic nozzles," *Flow, Turbulence and Combustion* 89(4) (2012) 601–625.

[31] T. S. Chyczewski, L. N. Long, P. J. Morris, "Numerical study of nozzle exit condition effects on jet development," *AIAA JOURNAL* 36 (6) (1998) 986–993.

[32] H. Yu, S. S. Girimaji, "Study of axis-switching and stability of laminar rectangular jets using lattice Boltzmann method," *Int. J. Comp. Math. Appli.* 55 (2008) 1611–1619.

[33] F. Krebs, F. Silva, D. Sciamarella, G. Artana, "A three-dimensional study of the glottal jet," *Exp. Fluids* 52 (2012) 1133–1147.

[34] M. Xu, J. Zhang, J. Mi, G. J. Nathan, P. A. M. Kalt, "PIV measurements of turbulent jets issuing from triangular and circular orifice plates," *SCIENCE CHINA Physics, Mechanics & Astronomy* 56(6) (2013) 1301–1309.

[35] M. Xu, J. Zhang, J. Mi, G. J. Nathan, P. A. M. Kalt, "Mean and fluctuating velocity fields of a diamond turbulent jet," *Chin. Phys. B* 22(3) (2013) 034701.

[36] M. El Hassan, A. Meslem, "Time-resolved stereoscopic PIV investigation of the entrainment in the near field of circular and daisy-shaped orifice jets," *Phys. Fluids* 22 (2010) 26.

[37] A. A. Sfeir, "The velocity and temperature fields of rectangular jets," *Int. J. Heat Mass Transfer* 19 (1976) 1289.

[38] A. A. Sfeir, "Investigation of three-dimensional turbulent rectangular jets," *AIAA J.* 17 (1979) 1055.

[39] W. R. Quinn, J. Militzer, "Experimental and numerical study of a turbulent free square jet," *Phys. Fluids* 31 (1988) 1017.

[40] M. R. Petersen, "A study of geophysical and astrophysical turbulence using reduced equations," Ph.D. Dissertation, University of Colorado (2004).

[41] S. B. Pope, *Turbulent Flows,* Cambridge University Press, Cambridge (2000).

[42] J. Smagorinsky, "General circulation experiments with the primitive equations: I. The basic equations," *Mon. Weather Rev.* 91 (1963) 99.

[43] H. Yu, S. S. Girimaji, L.-S Luo, "DNS and LES of decaying homogeneous isotropic turbulence with and without system rotations using lattice Boltzmann method," *J. Comput. Phys.* 209 (2005) 599.

[44] W. R. Quinn, "Passive near-field mixing enhancement in rectangular jet flows," *AIAA J.* 4 (1991) 515.

[45] A. Krothapalli, D. Baganoff, K. Karamcheti, "On the mixing of a rectangular jet," *J. Fluid Mech.* 107 (1981) 201.

[46] W. R. Quinn, "Turbulent free jet flows issuing from sharp-edged rectangular slots: The influence of slot aspect-ratio," *Exp. Therm. Fluid Sci.* 5 (1992) 203.